Defining the ordered pathway for ZAP-mediated RNA decay

Clément R. Bouton[1,7], Grega Gimpelj Domjanič[2,3,7], María José Lista[1,7], Rui Pedro Galão[1], Thomas Courty[1], Piotr Kwiatkowski[1], Harry D. Wilson[1], Peter W. S. Hill[1], Hannah E. Mischo[1], Anob M. Chakrabarti[4], Mario Poljak[3], Jernej Ule[2,5,6,*], Stuart J. D. Neil[1,*], Chad M. Swanson[1,8,*]

[1]Department of Infectious Diseases, King's College London, London, UK

[2]National Institute of Chemistry, Ljubljana, Slovenia

[3]Institute of Microbiology and Immunology, University of Ljubljana, Ljubljana, Slovenia

[4]UCL Respiratory, University College London, London, UK

[5]UK Dementia Research Institute at King's College London, London, UK

[6]Department of Basic and Clinical Neuroscience, Institute of Psychiatry Psychology & Neuroscience, King's College London, London, United Kingdom.

[7]These authors contributed equally

[8]Lead contact

*Correspondence: Jernej Ule (jernej.ule@kcl.ac.uk), Stuart Neil (stuart.neil@kcl.ac.uk), Chad Swanson (chad.swanson@kcl.ac.uk)

SUMMARY

Zinc-finger Antiviral Protein (ZAP)-mediated RNA decay (ZMD) restricts replication of viruses containing CpG dinucleotide clusters. However, why ZAP isoforms differ in antiviral activity and how they recruit cofactors to mediate RNA decay is unclear. Therefore, we determined the ordered events of the ZMD pathway. The long ZAP isoform preferentially binds viral RNA and has distinct binding motifs compared to the short isoform. The endoribonuclease KHNYN then cleaves viral RNA at positions of ZAP binding. The 5' cleavage fragment undergoes TUT4/TUT7-mediated 3' uridylation and degradation by DIS3L2. The 3' cleavage fragment is degraded by XRN1. ZAP and TRIM25 interact with KHNYN, TUT7, DIS3L2 and XRN1 in a RNase-resistant manner. Viral infection promotes the interaction between TRIM25 with these enzymes, leading to viral RNA decay while also decreasing the abundance of cellular transcripts. Overall, the long isoform of ZAP recruits key enzymes to assemble an RNA decay complex on viral RNA.

36 **INTRODUCTION**

37 A critical component of the innate immune response is the ability to distinguish between
38 self and non-self nucleic acids. The best characterized non-self RNA detection systems
39 include RIG-I, MDA5, PKR, OAS1-3 and ZBP1, which promote signaling that leads to
40 antiviral gene expression, cap-dependent translation inhibition, global RNA degradation
41 and cell death[1]. These pattern recognition receptors (PRRs) bind double-stranded RNA
42 (dsRNA), which acts as the pathogen-associated molecular pattern (PAMP). In contrast,
43 antiviral proteins that bind single-stranded RNA (ssRNA) often directly restrict viral
44 replication by inhibiting viral RNA translation or targeting it for decay[2]. Zinc-finger Antiviral
45 Protein (ZAP, also known as PARP13 or ZC3HAV1) is a paradigmatic example of a ssRNA-
46 binding protein critical for the cell autonomous innate immune response[3,4].

47

48 ZAP is encoded by an interferon-stimulated gene (ISG) that restricts diverse viruses
49 including retroviruses, alphaviruses, Ebola virus and human cytomegalovirus[5]. It has two
50 primary mechanisms for inhibiting viral infection: promoting viral RNA decay[3] and
51 inhibiting viral mRNA translation[6-8]. Several principles for the composition of ZAP-
52 response elements (ZREs) have been determined from synonymous genome recoding of
53 multiple viruses and structural/biochemical studies. CpG recoding can sensitize diverse
54 viruses to ZAP-mediated restriction[9-15], though UpA recoding has also been reported to
55 sensitize viral RNA to ZAP[11,13,16]. ZAP-mediated restriction requires the presence of at
56 least 15 CpGs, optimally separated by ~12-30 nucleotides (nt)[17], indicating that
57 multivalency is required for substrate recognition. Many mammalian RNA viruses have
58 low CpG abundance, likely due to evolutionary pressure from ZAP[9,18]. The RNA binding
59 domain (RBD) in ZAP contains four zinc finger motifs (ZnF1-4) and directly binds a single

60 CpG dinucleotide in pocket formed by ZnF2[3,10,12,19,20]. In addition to the CpG binding site,
61 RNA base-specific contacts between ZnF3 and ZnF4 have been identified and
62 C(n7)G(n)CG has been proposed as an optimal binding motif[12]. However, some regions
63 of viral RNA appear to be more sensitive to CpG-mediated ZAP restriction for unknown
64 reasons and high CpG abundance sometimes does not sensitize viral RNA to ZAP[14,21-25].
65 ZAP also regulates cellular transcript expression[26-29] and this, in addition to CpG DNA
66 methylation[30], has been proposed to contribute to the selective pressure against CpG
67 dinucleotide abundance in cellular genes[28,31,32]. However, little is known about the
68 composition of ZREs in cellular transcripts.
69
70 ZAP is the core of a multicomponent antiviral system. It has no enzymatic activity and
71 acts as a scaffold that recognizes target transcripts to recruit cofactors that inhibit
72 translation or mediate RNA decay[4]. The original model for ZAP-mediated RNA decay
73 (ZMD) was that it recruited enzymes that mediate decapping, deadenylation and
74 exonucleolytic degradation (Figure 1A)[33-36]. Specifically, this model proposed that ZAP
75 directly interacts with DDX17 to recruit DCP1A/DCP2 to mediate decapping and
76 subsequent 5'-3' decay via XRN1[34]. ZAP was also proposed to directly interact with PARN
77 and RNA exosome subunits to mediate deadenylation and 3'-5' decay[33,34]. In addition,
78 DHX30 was proposed to promote ZAP activity[37]. Subsequently, ZAP was shown to interact
79 with the E3 ubiquitin ligase TRIM25[38,39] and the endoribonuclease KHNYN[40]. This led to an
80 endonucleolytic decay model in which ZAP recruits KHNYN to internally cleave viral RNA
81 and this is promoted by TRIM25 through an unclear mechanism[4,40-42] (Figure 1B).
82 However, how KHNYN cleavage products are degraded is unclear in this model. Neither
83 model has been rigorously tested *in cellulo* and whether the two models can be

84 reconciled is unclear. The KHNYN paralog N4BP1 has also been implicated in ZMD and
85 these proteins have at least partially redundant activity for some transcripts[41,43,44].
86 Overall, the relative contribution of exonucleolytic versus endonucleolytic RNA decay
87 machinery and how they act in an ordered pathway remain poorly defined.
88
89 There are several ZAP isoforms, with ZAP-long (ZAP-L) and ZAP-short (ZAP-S) being the
90 most abundant[3,45,46] (Figure 1C). ZAP-S expression is induced by type I interferon while
91 ZAP-L is constitutively expressed[46,47], though both isoforms are induced by interferon γ[48].
92 Both ZAP-S and ZAP-L contain the RBD and a central domain that binds ADP-ribose[45,49,50].
93 ZAP-L also contains a catalytically inactive ADP-ribosyltransferase-like (ART-like) domain
94 and a C-terminal CaaX box that mediates S-farnesylation[45,51]. This post-translational
95 modification localizes ZAP-L to the cytoplasmic endomembrane system[27,51-53]. ZAP
96 isoforms have been proposed to have different functions[47,52] and, while ZAP-L has been
97 reported to have higher antiviral activity against several viruses than ZAP-S[45,46,52,53], the
98 mechanism for this is unknown.
99
100 There are multiple therapeutic applications arising from understanding the targeting
101 specificity of the ZAP antiviral system and how it mediates ZMD. TRIM25, ZAP, KHNYN and
102 N4BP1 target mRNAs delivered by lipid nanoparticles when they do not contain N^1-
103 methylpseudouridine modifications, highlighting its importance for therapeutic RNA
104 design[54]. Synonymous CpG-recoding of ZAP-resistant viral genomes has been shown to
105 be a novel way to develop live-attenuated viral vaccines[13-15,17]. Because ZAP expression is
106 downregulated in some types of cancer, ZAP-sensitive viruses have been proposed to be

107 used as oncolytic viruses because they would preferentially replicate in tumors with low
108 ZAP expression compared to healthy tissue[55].
109
110 In this study, we characterized the ZMD pathway to determine how ZAP interacts with
111 multiple enzymes to mediate viral RNA decay. Cells genetically engineered to only
112 express ZAP-L or ZAP-S show that, even though both isoforms contain the RBD, ZAP-L is
113 the predominant isoform that inhibits retroviral replication due to increased binding to
114 viral RNA and KHNYN. We then show that ZAP and TRIM25 interact with multiple RNA
115 decay enzymes including KHNYN, XRN1, TUT7 and DIS3L2 and order these enzymes into
116 a decay pathway. *In cellulo* identification of KHNYN cleavage sites shows that KHNYN
117 mediates endonucleolytic cleavage of the viral RNA in regions with high levels of ZAP
118 binding. The 5' cleavage fragment is 3' uridylated by the paralogs TUT4/TUT7 and then
119 degraded by DIS3L2. XRN1 degrades the 3' cleavage fragment. Viral infection increases
120 binding of TRIM25 to several components of this pathway and promotes regulation of
121 cellular genes by ZAP, TRIM25 and KHNYN. Overall, ZAP acts as a core scaffold for several
122 enzymes to mediate ZMD.
123
124 **RESULTS**
125 **Differential antiviral activity between ZAP isoforms correlates with binding viral RNA**
126 **and KHNYN**
127 ZAP restricts a wide range of viruses[5]. For this study, we used HIV-1 as a molecularly
128 tractable model virus to define the ordered events of the ZMD pathway. Wild-type HIV-1
129 (HIV-WT) is substantially depleted in CpG dinucleotides (Figure 1D) and the paucity of
130 these is due to strong selective pressure, likely from ZAP[9,32,56,57]. Mutations that introduce

131 a CpG in HIV-1 have a substantial fitness cost and the abundance of CpGs in HIV-1 *env* is
132 linked to disease progression[24,58,59]. Because HIV-1 is substantially depleted in CpGs,
133 these can be introduced through synonymous genome recoding to create HIV-CpG,
134 which contains a potent ZRE in *env* (Figure 1D)[9,40]. This allows isogenic viruses to be
135 analyzed under conditions in which ZAP restricts HIV-CpG but not HIV-WT (Figure 1E).
136 This restriction can be quantified, showing that HIV-CpG infectious virus production is
137 ~1% of HIV-WT (Figure 1E). Importantly, both viruses produce similar levels of infectious
138 virus when ZAP is knocked out. These paired viruses allow components of the ZAP
139 antiviral system to be characterized under conditions in which the *cis*-acting ZRE is either
140 absent or present in the virus, allowing ZMD substrate specificity to be determined in
141 each experiment.
142
143 The relative contribution of the two primary ZAP isoforms (Figure 1C) to ZMD is
144 controversial. While several papers have reported that ZAP-L is more active than ZAP-S,
145 others have proposed that ZAP-S, or shorter fragments of ZAP, are sufficient for antiviral
146 activity[24,41,45,46,51,52,60]. However, many of these experiments were performed by
147 overexpressing ZAP isoforms in wild-type cells or reconstituting ZAP isoforms in CRISPR
148 knockout cells, often by transient transfection, leading to non-physiological protein
149 levels. Furthermore, the mechanism by which ZAP-L may be more active than ZAP-S is
150 unclear. Therefore, we used a set of previously described HEK293T cells that were
151 CRISPR-engineered to express only ZAP-L or ZAP-S by targeting splice sites and poly(A)
152 sites in the endogenous *ZC3HAV1* locus[27]. These cells allow the antiviral activity of ZAP-L
153 or ZAP-S to be characterized without ectopic expression (Figure 1F). ZAP-L knockout
154 eliminated almost all ZAP antiviral activity against HIV-CpG while ZAP-S knockout had

155 only a minor effect (Figure 1G and S1A-B), demonstrating that, in this system, ZAP-L is the
156 essential mediator of viral restriction.
157
158 ZAP-L has previously been reported to interact more strongly with TRIM25 and KHNYN
159 than ZAP-S, though one or more of these proteins was often overexpressed in the
160 experimental conditions[38,53,61]. To determine if ZAP-L and ZAP-S preferentially interact
161 with TRIM25 or KHNYN when all the proteins are expressed from their endogenous locus,
162 we performed co-immunoprecipitation experiments in the wild-type, ZAP-L and ZAP-S
163 knockout cell lines. While ZAP-L or ZAP-S knockout did not substantially affect the
164 interaction between ZAP and TRIM25, ZAP-L knockout led to decreased ZAP interaction
165 with KHNYN (Figure 1H and S1C).
166
167 Because ZAP directly binds KHNYN through its N-terminal RBD[41,42], both ZAP isoforms
168 contain the KHNYN interaction domain. A possible mechanism for why depletion of ZAP-
169 L affected the ZAP-KHNYN interaction more than ZAP-S depletion may be that ZAP-L
170 assembles on the ZRE more efficiently than ZAP-S. To test this hypothesis, we used
171 iCLIP[62] to quantify the binding of each isoform to HIV-WT and HIV-CpG RNA (Figure 1I and
172 S1D-F). Three peaks were identified (Figure S1G), with the first at the 5' end of the viral
173 genome, the second in the 5' region of *env* covering the sequence that has been CpG
174 recoded, and the third in the 3' region of *env*. Peak 1 is ~250 nt wide in the 5' leader region
175 and *gag*, which contain a packaging element[63]. Peak 2, encompassing the CpG recoded
176 region in HIV-CpG *env* (Figure 1D, 475 nt long[40]), is ~800 nt long, indicating that ZAP
177 binding extends beyond the recoded region. Peak 3 is ~800 nt long and covers splice
178 acceptor 7 (SA7, nt 7904-7915)[64]. As expected, ZAP binding is most pronounced in Peak

179 2, covering the engineered ZRE. Consistent with ZAP oligomerization and the hypothesis
180 that multivalent binding of ZAP to multiple CpGs is required for its antiviral activity[17,41,65],
181 the iCLIP data implies assembly of ZAP molecules that cover wide, non-contiguous
182 regions on the viral RNA. Interestingly, the CpG clusters underlying Peak 1 and Peak 3,
183 which are present in both HIV-WT and HIV-CpG, show higher levels of binding in HIV-CpG
184 than HIV-WT RNA (Figure S1D and S1H), indicating that high ZAP binding to the
185 engineered region promotes additional ZAP recruitment at non-contiguous regions in the
186 viral RNA containing clustered CpGs. Of note, the thresholds used for this peak
187 identification were then used for all subsequent ZAP peak calling. In cells depleted for
188 ZAP-S, high levels of ZAP-L binding to HIV-CpG RNA were observed (Figure 1I, S1F and
189 S1I). By contrast, in ZAP-L knockout cells, ZAP-S showed low levels of RNA binding,
190 correlating with its low antiviral activity (Figure 1I, S1E and S1I). In sum, ZAP-L is the
191 primary antiviral isoform against HIV-CpG due to increased binding to HIV-CpG RNA and
192 a stronger interaction with KHNYN.
193
194 **ZAP-L and ZAP-S bind different motifs and regulate transcripts from different genes**
195 A potential evolutionary scenario for ZAP-regulated cellular transcripts is that ZAP
196 evolved to restrict viral replication and was then exapted to control cellular transcripts
197 containing similar sequences to the targeted viruses[66]. To determine why ZAP-L may bind
198 HIV-CpG RNA better than ZAP-S, we analyzed the iCLIP data for ZAP binding to cellular
199 transcripts. Motif analysis using PEKA[67] identified different motifs for ZAP-L and ZAP-S
200 (Figure 2A), with a UpA upstream of the CpG for 12 of the top 14 ZAP-L motifs, often in a
201 UACG or UANCG context (Figure S2A). This may at least partially explain why UpA
202 recoding of viral open reading frames can make a virus ZAP sensitive[11,13,16].

203

204 We then analyzed whether ZAP-L and ZAP-S regulated different cellular transcripts using
205 poly(A) RNA-seq (Table S1) and identified 156 and 240 genes encoding transcripts
206 specifically regulated by ZAP-L or ZAP-S, respectively, in HIV-WT infected cells. Gene
207 ontology (GO) analysis indicated that these are enriched for different
208 function/localization (Figure S2B-C). Genes encoding ZAP-L regulated transcripts are
209 enriched for plasma membrane, collogen-containing extracellular matrix, basement
210 membrane and cell adhesion (Figure S2B), indicating that they might be associated with
211 the plasma membrane or secreted. An example is the previously identified ZAP-regulated
212 gene TNFRSF10D (also known as TRAILR4), which acts as a decoy receptor to inhibit
213 TRAIL-mediated apoptosis[26,27]. Similar to HIV-CpG, transcript abundance from this gene
214 is preferentially regulated by ZAP-L (Figure 2B). In contrast, genes encoding ZAP-S
215 regulated transcripts are enriched for several transcription terms including transcription
216 factor AP-1 complex (Figure S2C). Several genes encoding components of the AP-1
217 transcription factor were upregulated specifically in ZAP-S knockout cells, including JUN,
218 JUNB, JUND and FOS (Figure 2C and S2D-F), and AP-1 activity was increased in ZAP-S
219 knockout cells (Figure 2D).

220

221 ZAP-L and ZAP-S have differential subcellular localization because ZAP-L has a C-
222 terminal CaaX box mediating S-farnesylation and membrane targeting[26,27,51-53]. ZAP-S is
223 diffuse in the cytoplasm while ZAP-L localizes to the endoplasmic reticulum,
224 endosomes, mitochondria and plasma membrane as well as the cytosol[26,27,51-53]. We
225 determined that HIV-CpG infection does not alter ZAP-L or ZAP-S localization, with both
226 showing the expected localization in uninfected and infected cells (Figure S2G). Because

227 ZAP-L partially localizes to the ER, we determined the proportion of genes encoding
228 transcripts regulated by ZAP-L or ZAP-S that contain a signal peptide sequence. 26% of
229 ZAP-L regulated genes and 13% of ZAP-S regulated genes are predicted to encode a signal
230 peptide (Figure 2E).
231
232 ZAP has been reported to regulate cellular transcript abundance through multiple direct
233 or indirect mechanisms including inhibiting microRNA-mediated repression after stress
234 or viral infection[68,69], modulating stress responses[27], modulating the type I interferon
235 response[29,31,52] and directly binding ZREs[26]. Therefore, we used the iCLIP data (Table S2)
236 to determine which genes regulated by ZAP may encode transcripts that are direct
237 targets. Transcripts from 16 of the 156 ZAP-L regulated genes and 42 of the 240 ZAP-S
238 regulated genes had defined ZAP binding peaks. Because ZAP-L is more antiviral than
239 ZAP-S, we focused on ZAP-L peaks. The average peak width for ZAP-L-regulated genes
240 was 246 nt (Table S2), which is long enough for multiple ZAP molecules to bind. Nine of
241 the 16 ZAP-L regulated genes with ZAP binding peaks had a predicted signal peptide or
242 known transmembrane domain, again showing that ZAP-L regulates transcripts that
243 localize to the ER and to other compartments. ZAP-L preferentially bound TNFRSF10D
244 RNA (Figure 2F) and there were two defined peaks in the transcript (Figure S3).
245 Interestingly, while UpAs are selected against in cellular transcripts expressed in the
246 cytoplasm[70], we observed abundant UpAs interspersed with CpGs in these peaks (Figure
247 S3) and a UACG motif in each peak that matches the core of several ZAP-L binding motifs
248 (Figure 2A and S2A).
249

250 **HIV-1 infection induces assembly of the ZAP-TRIM25-KHNYN complex and**
251 **regulation of cellular transcripts**

252 To determine if the presence of a substantial amount of ZAP substrate during HIV-CpG
253 infection affects the interaction between ZAP, TRIM25 and KHNYN, we performed co-
254 immunoprecipitation experiments in mock infected, HIV-WT and HIV-CpG infected HeLa
255 cells (Figure 3A-B). Interestingly, upon HIV-WT or HIV-CpG infection, there was an
256 increase in the RNase-resistant interaction between TRIM25 and KHNYN (Figure 3B and
257 S4A), even though the abundance of these proteins was unchanged. As expected[41],
258 TRIM25 knockout did not affect the interaction between ZAP and KHNYN (Figure 3C).
259 Therefore, viral infection appears to promote assembly of the ZAP-TRIM25-KHNYN
260 complex, but this does not require the strong ZRE present in HIV-CpG.

261

262 We then analyzed the effect of viral infection for ZMD of cellular transcripts using poly(A)
263 RNA-seq data from mock, HIV-WT or HIV-CpG infected Control, ZAP, TRIM25 or KHNYN
264 CRISPR cells (Table S3). Gene set enrichment analysis of differentially expressed genes
265 between HIV-WT or HIV-CpG infected cells compared to mock infected cells showed a
266 substantial change in transcripts associated with pathogen signaling including TNFα
267 signaling, inflammatory response, interferon-α and interferon-γ responses (Figure 3D-E).
268 This suggests that the increase in ZMD complex assembly correlates with an overall
269 antiviral response and we posited that HIV-1 infection may stimulate ZMD activity.

270

271 To determine how HIV-WT and HIV-CpG infection affect transcripts regulated by ZMD, we
272 focused on transcripts upregulated when ZAP, TRIM25 or KHNYN were knocked out. HIV-
273 WT or HIV-CpG infection increased the number of genes expressing transcripts

274 upregulated by ZAP or TRIM25 by ~2-3-fold and KHNYN-upregulated transcripts by ~5-
275 fold (Figure S4B-D). Analysis of genes encoding transcripts co-upregulated by ZAP,
276 TRIM25 and KHNYN showed an ~10-fold increase in both HIV-WT and HIV-CpG infected
277 cells compared to mock infected cells (Figure 4A-B). As expected from ZAP-L localization
278 and preferential regulation of transcripts encoding membrane proteins[26,27], the GO
279 analysis for ZAP-TRIM25-KHNYN co-upregulated genes showed that these were enriched
280 for encoding proteins associated with the endoplasmic reticulum (Figure 4C, Table S3).
281 Because ZAP has been reported to regulate a subset of interferon-repressed genes[31], we
282 also analyzed whether ZAP-TRIM25-KHNYN were required for repression of some genes
283 whose expression is downregulated after HIV-1 infection (Figure S5A). Exemplar genes
284 that encode transcripts regulated by ZAP, TRIM25 and KHNYN include the previously
285 reported ZAP-regulated gene ZMAT3[71] as well as HSPB8 and DIO2, which is
286 downregulated upon viral infection (Figure 4D-G and S5B-C).
287
288 ZAP, TRIM25 and KHNYN may also autoregulate ZAP-L abundance. ZAP-L expression has
289 previously been shown to increase in TRIM25 knockout cells after human
290 cytomegalovirus infection[72,73], though this was initially proposed to be due to changes in
291 alternative splicing of ZAP mRNA[72]. However, ZAP has recently been shown to bind a
292 region in the 3' UTR of ZAP-L[29], which may indicate that ZAP-L abundance is controlled by
293 TRIM25 and KHNYN through this ZRE. We confirmed that there is a strong ZAP binding
294 peak encompassing the ZAP-L mRNA 3' UTR that is not present in the ZAP-S mRNA (Figure
295 S5D-E). We also observed that ZAP-L expression increased in TRIM25 and KHNYN
296 knockout cells (Figure S5F-G). An isoform level analysis of poly(A) RNA-seq showed that
297 this correlates with increased ZAP-L mRNA abundance in HIV-infected TRIM25 and

298 KHNYN knockout cells (Figure S5H) This highlights that ZAP, TRIM25 and KHNYN
299 autoregulate ZAP-L expression. Overall, HIV-1 infection increases the interaction
300 between TRIM25 and KHNYN and this correlates with an increase in the number of genes
301 that are co-regulated by ZAP, TRIM25 and KHNYN, implying that an infectious stimulus
302 modulates the activity of ZMD on host transcripts.
303
304 Previous reports have shown that TRIM25 depletion decreases the interaction between
305 ZAP and Ebola virus RNA or a reporter transcript that is regulated by ZAP at the level of
306 translation[39,74]. Consistent with these reports, RNA-immunoprecipitation experiments
307 showed that ZAP binding to HIV-CpG RNA was moderately decreased in TRIM25 knockout
308 cells (Figure S6A). Analyzing ZAP iCLIP data for HIV-CpG infected TRIM25 knockout cells
309 also showed a moderate decrease in ZAP bound to viral RNA (Figure S6B-C). TRIM25
310 could directly regulate ZAP binding to viral RNA or depleting TRIM25 could sequester ZAP
311 on cellular transcripts that are unable to undergo decay, which would limit the pool of
312 ZAP available to bind exogenous transcripts such as viral RNA. We analyzed the effect of
313 TRIM25 depletion on ZAP binding to cellular transcripts in our iCLIP datasets and found
314 that 127 genes had increased normalized read abundance in TRIM25 CRISPR cells
315 compared to Control CRISPR cells (Figure S6D). Most of the 52 genes downregulated for
316 ZAP binding had low read abundance. ZAP (ZC3HAV1) was one of the top genes
317 upregulated for ZAP binding in TRIM25 knockout cells and a substantial increase in signal
318 was observed in the ZAP binding peak within the ZAP-L 3' UTR (Figure S6E), which could
319 reflect both the increased ZAP-L abundance in TRIM25 depleted cells and ZAP
320 accumulation on the transcript due to reduced decay. Taken together, the decreased ZAP
321 binding we and others have observed on exogenous transcripts when TRIM25 is depleted

322 could be due to increased ZAP binding on cellular transcripts and therefore a smaller
323 pool of ZAP available to target viral RNA.
324
325 While TRIM25 has been proposed to regulate the specificity of ZMD in addition to its
326 potency[41], we did not observe any substantial change in ZAP antiviral activity against HIV-
327 WT in TRIM25 knockout cells (Figure S5G). Furthermore, the relative position of ZAP
328 binding to HIV-CpG RNA did not change in TRIM25 knockout cells (Figure S6B, Spearman
329 correlation of relative crosslink signal at each nucleotide in CRISPR control and TRIM25
330 knockout cells = 0.92). PEKA analysis of iCLIP data for cellular transcripts in CRISPR
331 control and TRIM25 knockout cells showed that the UpA + CpG motifs identified for ZAP-
332 L were enriched in both conditions and there was no substantial change in the number of
333 cellular transcripts with ZAP binding peaks (Figure S6F-G, Table S4). Therefore, TRIM25
334 appears to moderately regulate ZAP binding to viral RNA, possibly due to ZAP being
335 sequestered on cellular RNA when TRIM25 is depleted, but does not change the ZAP
336 targeting specificity.
337
338 **XRN1 degrades the 3' fragment after endonucleolytic cleavage**
339 We then sought to test the exonucleolytic and endonucleolytic decay models for ZMD
340 (Figure 1A-B). One prediction of the ZMD endonucleolytic model (Figure 1B) is that
341 KHNYN binding would be present in regions with clustered CpGs. Therefore, we used
342 iCLIP to map KHNYN binding sites on HIV-CpG RNA. Because we have not found an
343 antibody that efficiently immunoprecipitates KHNYN, we identified KHNYN binding sites
344 on viral RNA using a previously characterized stable cell line expressing an active KHNYN-
345 GFP fusion protein[61]. KHNYN had substantial binding within areas of high CpG

346 abundance, including the CpG recoded region of HIV-CpG (Figure 5A). It also bound
347 motifs containing a CpG (Figure S7A). As KHNYN has no known RNA binding
348 specificity[42,44], this supports the hypothesis that ZAP recruits KHNYN to target RNA.
349 Interestingly, motifs enriched around KHNYN crosslink sites also contain UpA
350 dinucleotides, including UACG motifs (Figure S7A).
351
352 For the ZMD exonucleolytic decay model (Figure 1A), ZAP has been reported to interact
353 with PARN, the exosome complex (EXOSC5, EXOSC7), DCP2, XRN1, DDX17 and DDX30[33-
354 35,37,75]. In addition, ZAP has been reported to interact with components of the CCR4-NOT
355 deadenylation complex[76,77]. The endonucleolytic and exonucleolytic models could be
356 reconciled if these are parallel pathways or if some of the exonucleolytic model
357 components are required for RNA decay after endonucleolytic cleavage. To identify
358 whether any of these proteins are required for ZAP antiviral activity on HIV-CpG, we
359 depleted them using RNAi. While siRNA-mediated depletion of ZAP, TRIM25 and KHNYN
360 increased HIV-CpG infectious virus production, none of the ZAP cofactors implicated in
361 the exonucleolytic model had an effect (Figure S7B-E), consistent with a previous study[9].
362 This suggests that the endonucleolytic pathway is dominant for restricting HIV-CpG,
363 leading to a cleaved viral genome that can't be translated or packaged into virions.
364 However, exonucleases could be required to degrade viral RNA fragments after KHNYN
365 cleavage. Therefore, we designed a probe to potentially identify the 3' cleavage fragment
366 of HIV-1 RNA with the presumption that many KHNYN cleavage sites will be near the
367 major ZAP binding site in the CpG-recoded region (probe 2 (p2) in Figure 5B). Of note, due
368 to the complex HIV-1 alternative splicing program[64], only the unspliced and singly spliced
369 HIV-1 transcripts will contain the ZAP-sensitive CpG-recoded region and the fully spliced

370 RNAs are not subject to ZMD[9,40] (Figure 5B). To quantify only ZAP-sensitive transcripts, p2
371 was designed to span SA7, which is the last sequence that is specific to the singly and
372 unspliced transcripts. Notably, this sequence is within ZAP binding peak 3 (Figure 1I).
373 RNAi-mediated depletion of CNOT1, PARN, EXOSC3, EXOSC5, EXOSC7, DDX17 or
374 DHX30 did not affect HIV-CpG RNA abundance using the probe for the 3' fragment (Figure
375 S7F-G), but depletion of the 5'-3' exonuclease XRN1 led to a significant increase in
376 abundance (Figure 5C).
377
378 To determine if ZAP and TRIM25 interact with XRN1, we performed co-
379 immunoprecipitation experiments in the absence and presence of HIV-1 infection (Figure
380 5D-E and Figure S7H). Both proteins interact with XRN1 in a RNase-resistant manner and
381 the interaction between TRIM25 and XRN1 is stimulated by either HIV-WT or HIV-CpG
382 infection. Similar to the interaction between ZAP and KHNYN, TRIM25 is not required for
383 ZAP to interact with XRN1 (Figure S7I). Overall, we hypothesize that a ZAP-TRIM25
384 complex recruits XRN1 to degrade the 3' cleavage product.
385
386 An important prediction of the endonucleolytic model for ZMD is that internal cleavage
387 sites should be identified when degradation of the cleavage products is inhibited.
388 Therefore, we used 5' RACE to identify potential cleavage sites in XRN1 depleted cells
389 using a HIV-1 specific primer at the 3' end of the viral genome (Figure 5B). Visualizing the
390 RACE products on an agarose gel showed that a novel band appeared for the control
391 siRNA HIV-CpG sample (3' cleavage fragment in Figure 5F). When ZAP was depleted, this
392 band was not present and the abundance of the band increased when XRN1 was knocked
393 down. Therefore, we hypothesized that this band could be a KHNYN cleavage product

394 that is further degraded by XRN1. To map the cleavage sites, we used Oxford Nanopore
395 sequencing for the total 5' RACE reactions and identified the 5' end of each read. In XRN1
396 knockdown cells, HIV-CpG 5' ends clustered in ZAP binding Peaks 2 and 3 (Figure 5G).
397 This indicates that ZAP likely recruits KHNYN to these sites to mediate cleavage and that
398 the ZAP binding in Peak 3 is sufficient for KHNYN cleavage. This also suggests that the
399 increase in 3' cleavage fragment abundance when XRN1 is depleted (Figure 5C) may be
400 underestimated because probe 2 (Figure 5B) covers the site of endonucleolytic cleavage
401 in ZAP binding Peak 3. However, as described above, this is the most distal 3' sequence
402 that the probe can cover and still be specific for the ZRE-containing RNA. Importantly, the
403 5' RACE assay has a 3' bias in that if KHNYN cuts multiple times in a transcript, the 5' end
404 closest to the RACE primer will be identified, so the relative frequency of cleavage sites
405 in Peaks 2 and 3 should not be directly compared. The sequence underlying Peak 3 is
406 identical between HIV-WT and HIV-CpG, suggesting that ZAP binding in Peak 2 not only
407 promotes ZAP binding in Peak 3 (Figure S1D and H) but that this binding is functional,
408 leading to endonucleolytic cleavage.
409
410 We identified 153 high confidence cleavage sites spanning nt 6007-8299. Interestingly,
411 68 of these were within a 92 nt region from nt 6261-6352 in which almost every nucleotide
412 was a high confidence cleavage site (Figure S8A-B). Within this region, both CpG and UpA
413 are enriched (observed/expected CpG = 1.72, UpA = 1.48). There are nine UACG motifs in
414 the HIV-CpG genome, seven of which have been introduced by CpG-recoding, and three
415 of these are found within the 92 nt region (Figure S8B). There was strong ZAP iCLIP signal
416 and moderate KHNYN iCLIP signal (Figure S8A), which may be indicative of active
417 cleavage and a short KHNYN residence time on the RNA. Therefore, frequent

418 endonucleolytic cleavage correlated with high levels of ZAP binding in a region containing
419 UACG motifs, consistent with the sequence within several of the top ZAP-L iCLIP motifs
420 (Figure 2A and S2A).
421
422 **The 5' cleavage fragment is 3' uridylated by TUT4/7 and then degraded by DIS3L2**
423 To determine how the 5' cleavage fragment was degraded, we set up a qRT-PCR assay
424 with a primer-probe set upstream of Peak 2 (probe 1 (p1) in Figure S9A) and then screened
425 the RNA degradation proteins linked to ZAP to determine if they regulate the abundance
426 of this fragment. Surprisingly, depletion of three exosome subunits, EXOSC3, EXOSC5 or
427 EXOSC7, had no effect on the abundance of the 5' cleavage fragment (Figure S9B).
428 Depletion of CNOT1, PARN, XRN1, DDX17 or DHX30 also had no effect, indicating that
429 degradation of the 5' fragment was not regulated by known ZAP-interacting proteins
430 linked to RNA decay. Therefore, we performed 3' RACE to identify the location and identity
431 of the 3' ends of the 5' cleavage fragment (Figure 6A and S9A). A potential 5' cleavage
432 fragment was observed specifically in cells infected with HIV-CpG and was not present
433 when ZAP was depleted. We cloned this band and sequenced seven clones using Sanger
434 sequencing. Interestingly, reads terminated within ZAP binding Peak 2 and several had
435 non-templated uridines at the 3' end (Figure 6B). This result raised the possibility that the
436 5' fragment was modified by 3' uridylation.
437
438 Several members of the TENT family of polymerases add non-templated nucleotides at
439 the 3' end of transcripts and TUT1, TUT4 and TUT7 are three proteins that specifically add
440 non-templated uridines[78]. TUT1 is a nuclear protein that had no effect when it was
441 depleted (Figure 6C). In contrast, depletion of two cytoplasmic paralogs that are often

442 functionally redundant, TUT4 and TUT7, promoted an increase in the abundance of the 5'
443 cleavage fragment (Figure 6C and S9C). As expected, TUT4/7 depletion had no effect on
444 infectious virus production, indicating that it acts downstream of endonucleolytic
445 cleavage (Figure S9D), or the abundance of the 3' cleavage fragment (Figure S9E). We
446 then analyzed whether ZAP and TRIM25 interacted with TUT7. Both proteins interacted
447 with it in an RNase-resistant manner and this interaction was increased in the presence
448 of HIV-WT or HIV-CpG infection (Figure S9F-H). The interaction between ZAP and TUT7
449 was not altered in TRIM25 knockout cells (Figure S9I).
450
451 DIS3L2 is an exosome-independent, 3'-5' exoribonuclease that degrades transcripts with
452 3' terminal uridylation[79-81]. Depleting its expression increased expression of transcripts
453 using the 5' probe but not the 3' probe (Figure 6C and S10A-B), indicating that it is required
454 to degrade the 5' KHNYN cleavage fragment. DIS3L2 depletion does not affect HIV-CpG
455 infectious virus production (Figure S10C), indicating that it also acts after
456 endonucleolytic cleavage. ZAP and TRIM25 interact with DIS3L2 in an RNase-resistant
457 manner, and the interaction between TRIM25 and DIS3L2 is increased by HIV infection
458 (Figure S10D-F). Knocking out TRIM25 did not affect the interaction between ZAP and
459 DIS3L2 (Figure S10G). We then used 3' RACE-seq to map internal cleavage sites in HIV-
460 CpG after DIS3L2 depletion and found that they are concentrated in ZAP binding Peak 2
461 (Figure 6D). We also determined proportion of 3' uridylation and length. When DIS3L2 is
462 depleted, ~50% of the reads have at least one non-templated nucleotide and a
463 substantial portion have at least 10 non-templated nucleotides (Figure 6E). These non-
464 templated nucleotides are highly enriched in uridine, indicating a poly-uridine tail. In
465 contrast, when ZAP is depleted, few reads contain non-templated tails and the strong

466 enrichment for uridine is not present. These data indicate that after KHNYN cleavage, the
467 5' cleavage products of the viral RNA become 3'-polyuridylated by TUT4/7 and are then
468 degraded by DIS3L2.
469
470 Overall, these experiments lead to a comprehensive model for ZMD (Figure 7). ZAP-L
471 forms a complex with TRIM25 and KHNYN to direct KHNYN-mediated endonucleolytic
472 cleavage in regions of high ZAP binding. After cleavage, ZAP and TRIM25 interact with
473 additional RNA decay machinery to mediate degradation of the resultant fragments.
474 XRN1 degrades the 3' cleavage fragment. The 5' cleavage fragment is 3' uridylated by
475 TUT4/7 and then degraded by DIS3L2. This allows the entire viral RNA to be degraded after
476 its recognition by ZAP.
477
478 **DISCUSSION**
479
480 Determining how ZAP selects specific transcripts for decay is essential to utilize it for
481 novel vaccine and oncolytic virus development and to prevent it from targeting
482 therapeutic RNAs. A simple model for ZMD specificity is that ZAP binds CpG
483 dinucleotides through ZnF2 in its RBD and regions containing clustered CpGs are
484 sufficient to mediate specificity[9,10,12,17]. Supporting this model, ZAP has high affinity for
485 RNAs containing a CpG dinucleotide and CpG recoding can sensitize diverse viruses to
486 ZAP-mediated restriction[9-14]. However, some regions of viral RNA appear to be more
487 sensitive to CpG-mediated ZAP restriction and high levels of CpG abundance sometimes
488 does not sensitize viral RNA to ZAP[14,21-25]. In particular, this has been shown for
489 synonymous recoding of influenza virus to develop novel live attenuated virus vaccines.

490 Some CpG recoding strategies have led to ZAP-mediated attenuation and in other cases
491 substantial increases in CpG abundance have not sensitized the virus to ZAP[14,22,82,83]. In
492 addition, UpA recoding has been reported to sensitize viral RNA to ZAP[11,13,16]. Our data
493 indicate that while both ZAP-L and ZAP-S bind motifs containing a CpG, ZAP-L binds
494 motifs that also contain an upstream UpA. This may explain why UpA recoding can
495 sensitize a virus to ZAP-mediated restriction. Many viral genomes are depleted in both
496 CpG and UpA dinucleotides[70] and introducing both into such viruses may increase their
497 sensitivity to ZAP-L. Supporting this hypothesis, a study published while this manuscript
498 was under revision compared CpG to CpG + UpA recoding for West Nile virus and found
499 that CpG + UpA recoding had superior pre-clinical vaccine characteristics[15].
500
501 Why ZAP-L and ZAP-S bind different RNA sequence motifs given they have the same RBD
502 remains unclear, but it is likely directly or indirectly regulated by the ART-like domain and
503 C-terminal S-farnesylation. Adding a CaaX box at the C-terminus of ZAP-S partially
504 increases its antiviral activity, and this correlates with its localization to the
505 endomembrane system[52,53]. However, transferring the CaaX box to the ZAP-S does not
506 restore full antiviral activity and the ART-like domain likely has a role as well, though its
507 function is not known. While ZAP-S is predominately cytosolic, ZAP-L localizes to multiple
508 organelles in the endomembrane system as well as the cytosol[26,27,51-53] and may target
509 transcripts in several cytoplasmic regions. Recent studies have highlighted that cellular
510 transcripts associate with multiple compartments in the endomembrane system
511 including the ER, outer mitochondrial membrane, endosomes and TIS granules[84-86]. High
512 resolution studies will be required to determine how ZAP-L and ZAP-S subcellular
513 localization controls transcripts that localize in specific cytoplasmic compartments.

514 ZAP-L and ZAP-S could bind different motifs through interacting with different cofactors
515 or due to conformational changes, possibly regulated by membrane binding. The ZAP
516 RBD has four zinc fingers and RNA binding has been observed in regions outside of the
517 ZnF2 CpG binding pocket[12,20,87]. In addition, it has been reported to interact with many
518 other RNA binding proteins[4]. How ZnF1, ZnF3 and ZnF4 in the ZAP RBD and other ZAP-
519 interacting RNA binding proteins contribute to specific RNA targeting and ZMD activity
520 will require future studies.
521
522 While we focused on ZAP-L-mediated RNA decay in this study, ZAP-S has several reported
523 roles and how RNA binding differences between ZAP-L and ZAP-S regulate different
524 aspects of cellular function remain an important area for further investigation. ZAP-S has
525 been shown to regulate RIG-I signalling[47], interferon mRNA abundance[52] and the
526 unfolded protein response during cellular stress[27] as well as restrict SARS-CoV-2 by
527 inhibiting programmed ribosomal frameshifting[8]. An interesting implication for how ZAP-
528 L and ZAP-S regulate different transcripts is how this contributes to diseases in which ZAP
529 expression is dysregulated, such as some types of cancer[26,55,88]. While several studies
530 have analyzed ZAP-regulated transcripts in the context of knocking out both ZAP-S and
531 ZAP-L[26,28,29], here we have extended a previous study[27] showing differential transcript
532 targeting by the two isoforms. ZAP-L regulation of TNFRSF10D and ZAP-S regulation of AP-
533 1 activity are two examples of how ZAP isoforms may impact tumorigenesis. While the
534 functional consequences of alterations in ZAP-L or ZAP-S expression for cellular
535 transcripts requires further study, future characterization of the role of ZAP in tumors
536 should consider isoform specific changes as well as overall changes in ZAP expression.
537

538 In this study, we have focused on the role of KHNYN for mediating the endonucleolytic
539 cleavage event but N4BP1 may also cleave ZAP-targeted RNA. N4BP1 is a core vertebrate
540 ISG[89] and is functionally redundant with KHNYN for some transcripts[41,43,44]. N4BP1 targets
541 specific mRNAs[90] and whether N4BP1 and KHNYN have differential transcript specificity
542 is not clear. While the ZAP RBD binds the KHNYN CUE-like domain[41], several of the
543 residues in KHNYN that mediate this interaction are not conserved in the N4BP1 CUE-like
544 domain[61]. This implies that there may be further interactions between ZAP and
545 KHNYN/N4BP1 or that they interact with other components of the ZAP antiviral system[54].
546 How KHNYN is regulated so that it only cleaves at sites directed by ZAP is unclear, though
547 it shows specificity for targeting ZAP-sensitive viruses even when overexpressed[21,40].
548 KHNYN abundance on a per molecule basis is substantially lower than ZAP[61] and it is
549 likely a limiting factor for antiviral activity[40]. Structural studies will be required to
550 understand how multiple ZAP molecules assemble on a ZRE and interact with KHNYN to
551 provide targeted decay. Other endonucleases in the same gene family as KHNYN, such
552 as ZC3H12A[91], are controlled through a combination of post-translational modifications
553 that regulate their stability and interaction with other proteins and this may be important
554 for KHNYN activity as well. Furthermore, KHNYN is highly active in the presence of
555 manganese[92], which can be released into the cytosol after viral infection[93], and local
556 manganese abundance may also regulate its activity.
557
558 One of the major unresolved questions for ZMD is how TRIM25 regulates ZAP activity.
559 TRIM25 has ubiquitylation/ISGylation activity[38,39,74,94], multimerizes through its N-terminal
560 RING domain[41,95] and also binds RNA[96-98]. All of these functions have been proposed to
561 regulate its antiviral activity and an interaction between TRIM25 and TUT4 has also been

562 reported to control let-7 microRNA decay[99]. Consistent with previous reports[39,74], we
563 found that TRIM25 depletion decreased ZAP binding to viral RNA. However, this effect is
564 moderate and may be due to an increased occupancy of ZAP on cellular transcripts,
565 which could decrease the pool of ZAP available to target exogenous RNA. Because
566 TRIM25 binds both cellular and viral RNA[96-102], it could act as a co-reader with ZAP to
567 ensure target specificity[29]. Alternatively, it could promote multimeric ZAP complex
568 formation through RING domain dimerisation[41] or modify a component of the ZAP
569 antiviral system with ubiquitin or ISG15[38,39,74,94]. Specific mutations in TRIM25 that isolate
570 different activities will be required to determine how it regulates ZAP antiviral activity,
571 though this is challenging since TRIM25 binds ssRNA and dsRNA through multiple sites
572 and RNA binding, multimerization and E3 ubiquitin ligase activity are linked[96-98]. HIV
573 infection increased TRIM25 interaction with KHNYN, XRN1, TUT7 and DIS3L2 and this
574 correlates with increased repression of cellular transcripts by ZAP, TRIM25 and KHNYN.
575 Importantly, this occurred for both HIV-WT and HIV-CpG infection, indicating that viral
576 RNA substrate is not required for increased TRIM25 interaction with RNA decay enzymes.
577 While TRIM25 RNA binding activity is regulated by pH[54] and local pH changes caused by
578 viral infection could modulate its interaction with RNA, possibly through virion fusion with
579 endosomes or alterations in mitochondria, we note that the interaction between TRIM25
580 and the RNA decay enzymes was RNase-resistant. Therefore, additional changes in
581 TRIM25 in the context of viral infection, such as post-translational modifications, may
582 control the ZAP antiviral system by altering the TRIM25 interactome.
583
584 We have shown that depletion of the 5' RNA decay fragment requires TUT4/7, indicating
585 that uridylation after an internal cleavage event is required for complete viral RNA decay.

586 While 3' uridylation has previously been linked to restriction of viruses[103,104] and LINE-1
587 retrotransposition[105], this has predominately been proposed to occur at the 3' end of the
588 transcript. One reason why 3' uridylation might be critical for degradation of viral RNA is
589 that it can recruit DIS3L2, which can degrade structured RNA[106]. Higher order RNA
590 structures are common in viral RNA, especially positive strand RNA virus genomes. For
591 example, the HIV-1 genome has several regions of RNA structure[107] and the ability of
592 DIS3L2 to degrade structured RNA may be required to completely destroy the viral RNA.
593 It should be noted that many ZAP-sensitive viruses produce viral RNA that comprise a
594 substantial percentage of total poly(A) RNA[108-110]. Complete degradation of the RNA may
595 be important to prevent partially degraded RNA species from sequestering cellular RNA
596 binding proteins, stimulating the innate immune response or otherwise dysregulating
597 cellular RNA metabolism.
598
599 **LIMITATIONS OF THE STUDY**
600 While the iCLIP experiments demonstrate ZAP binding over three broad regions in HIV-
601 CpG RNA, this technique does not determine the number and location of ZAP molecules
602 bound to HIV-CpG at individual transcript resolution. Therefore, while we hypothesize
603 that ZAP multivalent binding is important for target specificity, which is supported by
604 previous genetic studies[9,17], the iCLIP experiments do not show this definitively.
605 Furthermore, while the RACE-seq experiments show that ZAP-specific internal cleavage
606 sites correlate with regions of ZAP binding on HIV-CpG, we cannot correlate cleavage
607 sites with specific ZAP binding sites on an individual transcript basis.
608
609 **METHODS**

610 **Cell lines, viruses and infection**

611 HEK293T CRISPR cells[27], HeLa, HeLa CRISPR cells[40,61] and TZM-bl cells[111-113] were
612 maintained in high-glucose DMEM supplemented with GlutaMAX (Thermo Fisher
613 Scientific), 10% fetal bovine serum, 100 U/mL penicillin and 100 µg/mL streptomycin and
614 grown with 5% CO2 at 37°C.

615

616 HIV-WT and HIV-CpG stocks were produced by co-transfecting pHIV-WT[114] or pHIV-CpG[40]
617 with pVSV-G[115] into HEK293T CRISPR ZAP cells, harvesting at 48h post-transfection and
618 titering on TZM-bl cells as described below. The sequences of HIV-WT and HIV-CpG are
619 available in the National Center for Biotechnology Information Nucleotide Database with
620 Accession MN685337 and MN685350, respectively.

621

622 Unless otherwise stated, cells were infected at MOI=3. The medium was replaced 18
623 hours (h) post-infection. Cell lysates and supernatants were collected at 48 hours post-
624 infection. Cell-free supernatants were produced by centrifugation at 300×*g* for five
625 minutes.

626

627 **siRNA transfection and infection**

628 siRNA were purchased from Horizon Discovery and transfected using Lipofectamine
629 RNAiMAX (Invitrogen). siRNAs were reverse-transfected with 1 µL lipofectamine at 25 nM
630 final concentration for 90,000 HeLa cells in a 24-well plate. 24 hours later, the medium
631 was replaced, and cells were transfected again with siRNA at 25 nM final concentration
632 with 1µL lipofectamine. 6-8 hours later, cells were infected with HIV-1 at MOI=3. The

633 medium was replaced 18 hours post-infection. Supernatant and cell lysates were
634 collected 48 hours post-infection as described above.
635
636 **TZM-bl infectivity assay**
637 The TZM-bl cell line was used to quantify the amount of infectious virus[111-113]. $1x10^4$ cells
638 per well were seeded in 96-well plates and infected by incubation with virus stocks or
639 supernatants of infected cells. At 40-48 hours post-infection, cells were lysed and
640 infectivity was measured by β-galactosidase expression using the Galacto-Star assay
641 system as per the manufacturer instructions. β-galactosidase activity was quantified as
642 relative light units per second using a PerkinElmer luminometer.
643
644 **Immunoblotting**
645 Cell lysates for immunoblotting were prepared in Laemmli buffer. Virions were pelleted
646 from culture supernatant by centrifugation at 20,000 x *g* for 2 hours at 4°C through a 20%
647 sucrose cushion in phosphate-buffered saline (PBS). Viral pellets were resuspended in
648 2x Laemmli buffer. Samples were boiled for 10 min at 95°C, separated on 8-16% gradient
649 precast gels (BioRad; Millipore) and then transferred to nitrocellulose or PVDF
650 membranes (Amersham). Membranes were briefly rinsed in PBS then blocked in blocking
651 buffer (PBS, 5% non-fat milk, 0.1% Tween 20) for 30 minutes at RT. Membranes were
652 incubated with primary antibodies diluted in blocking buffer at 4°C overnight, then
653 washed 3 times for 5 min in PBS-T (PBS, 0.1% Tween 20), then incubated with secondary
654 antibodies diluted in blocking buffer for 1h at RT, then washed for 3 times for 5 min in PBS-
655 T. Membranes were imaged using an Odyssey FC (LI-COR) measuring secondary
656 antibody fluorescence, or using Amersham ECL Prime Western Blotting Detection

657 reagent (Cytiva) for HRP-linked antibodies with an Amersham ImageQuant 800 (Cytiva).
658 Antibodies used in this study are reported in the STAR methods table.
659
660 **Coimmunoprecipitation**
661 1.5 mg Dynabeads protein A (Invitrogen) per sample were incubated in lysis buffer (0.5%
662 Nonidet P 40 (NP40) substitute, 10mM HEPES pH=7.5, 150mM KCl, 3mM MgCL2,
663 protease inhibitor) supplemented with 5% BSA for 30 min at RT and under gentle
664 agitation. 4 µg of antibody per sample was bound to the beads for 30 min at RT and under
665 gentle agitation. The unbound antibody was then washed off and the beads were
666 resuspended in 50 µL lysis buffer per sample. Cells cultivated in a 10-cm dish were lysed
667 on ice in 1mL lysis buffer. In case of infected cells (MOI=3), cells were lysed 48 hours post-
668 infection. Lysates were gently mixed on a rotator for 30 min at 4°C, then centrifuged at
669 20,000 ×*g* for 10 min to pellet the nuclear fraction. 75 µL of the post-nuclear supernatant
670 was saved as the input lysate and mixed with 1 volume of Laemmli buffer. 900 µL of the
671 remaining post-nuclear supernatant was incubated with the prepared beads under
672 gentle agitation over night at 4°C. The samples were then washed four times in wash
673 buffer (0.05% Nonidet P 40 substitute, 10mM HEPES pH=7.5, 150mM KCl, 3mM MgCL2,
674 protease inhibitor) before being resuspended in 90 µL Laemmli buffer. For experiments
675 including an RNase I treatment, the samples were washed twice in wash buffer after the
676 overnight incubation with the prepared beads, then resuspended in 100 µL wash buffer.
677 The samples were incubated with 300 U RNase I for 30 min at 37°C and washed three
678 times in wash buffer before being resuspended in 90 µL Laemmli buffer. Input lysates and
679 samples were analyzed by immunoblotting as described above. Coimmunoprecipitation
680 and pull-down immunoblots were quantified using Image Studio (LI-COR Biotech).

681 Relative coimmunoprecipitation efficiency was calculated as the ratio of
682 coimmunoprecipitation to pulldown then normalized to the same ratio calculated in
683 control conditions.
684
685 **qRT-PCR**
686 Total RNA was extracted using the RNeasy Mini Kit (Qiagen). cDNA was synthesized using
687 the High-Capacity cDNA RT kit (Applied Biosystems) following the manufacturer's
688 instructions. cDNA was diluted 20 times in RNase-free water and quantified by qPCR
689 using Applied Biosystems TaqMan Universal PCR Master Mix (Applied Biosystems) in a
690 QuantStudio 5 qPCR System (Applied Biosystems). Relative cDNA quantities were
691 determined using the ΔΔCt method. The primer-probe set for these experiments are in
692 the 3' end of *gag* and are reported in the STAR methods table.
693
694 **RNA Immunoprecipitation**
695 HeLa CRISPR Control/TRIM25/KHNYN cells[40] were plated in 6-well plates and
696 transfected using TransIT-LT1 transfection reagent with 500 ng of HIV-WT or HIV-CpG
697 proviral DNA, and medium was replaced 4-6 hours later. 48 hours post-transfection cells
698 were washed with PBS prior to UVC crosslinking (254nm) with 400mJ/cm2 using a UV
699 Stratalinker 2400 (Stratagene). Cells were then pelleted, lysed with RIPA buffer (50mM
700 Tris-HCl pH 7.4; 150mM NaCl; 0.1% SDS; 0.5% sodium deoxycholate, 1% Nonidet P 40
701 substitute and protease inhibitors) and then sonicated. Cleared lysates were
702 immunoprecipitated overnight at 4°C with anti-ZAP antibody (Abcam) and Dynabeads
703 protein G (Invitrogen). Following 3 washes with RIPA buffer, beads were resuspended in
704 100 µl of RIPA and boiled for 10min to decouple protein/RNA complexes from the beads.

705 Finally, input and pulldown samples were incubated with proteinase K (Thermo Fisher)
706 for 1 hr at 37°C, and then boiled for 10 minutes to inactivate the enzyme. Samples were
707 stored at -20°C for downstream RNA extraction and qRT-PCR analysis.
708
709 RNA from the input and pulldown samples was extracted using QIAzol (QIAGEN). cDNA
710 synthesis was performed using the High-Capacity cDNA RT kit as described above. Of the
711 final reaction, 5 µl were subjected to qPCR using the primer/probe sets for human
712 GAPDH and HIV-1 genomic RNA reported in the STAR methods table. Serial dilutions of
713 HIV-WT proviral DNA were used in standard curves as calibrator for quantification of HIV-
714 1 RNA copies in the pull-down fractions.
715
716 **AP-1 reporter assay**
717 One day prior to transfection, HEK293T cells were seeded in a 24-well plate at a density
718 of $2x10^5$ cells per well. Approximately 8 h later, cells were treated with 50 ng/mL phorbol
719 12-myristate 13-acetate (PMA; Peprotech) and incubated overnight. The following day,
720 cells were transfected with a DNA mix containing 85 ng of the AP-1 firefly luciferase
721 reporter plasmid[116] and 15 ng of the Renilla luciferase control plasmid (pGL4.74
722 hRluc/TK; Promega cat. #E6921) using 1 µL Lipofectamine 2000 (Invitrogen). Cells were
723 incubated for 24 h and then lysed in 1x Passive Lysis Buffer (Promega). Dual-Luciferase
724 Reporter Assay (Promega) was performed according to the manufacturer's instructions,
725 and luminescence was measured using a VICTOR X3 microplate reader (Perkin Elmer).
726 Data was normalized as fold-change (ZAP knockout over control) by calculating the ratio
727 of firefly to Renilla luminescence, with values from the control cell line set to 1.
728

729 **Immunofluorescence and RNA FISH**

730 Cells were seeded on poly-L-lysine coated plates and infected with HIV-WT or HIV-CpG
731 (MOI=1) then fixed in 3.7% (vol./vol.) formaldehyde at 24hpi. Cells were first
732 immunostained for ZAP and the ER marker RTN4, then hybridized with Stellaris probes
733 targeting unspliced HIV RNA (add ref https://doi.org/10.7554/eLife.62470) using Stellaris
734 FISH buffers following the Stellaris protocol for sequential immunofluorescence (IF) +
735 Stellaris RNA FISH in adherent cells (Biosearch Technologies). Images were acquired
736 using a Nikon AXR NSPARC microscope at the Nikon Imaging Centre, King's College
737 London.

738

739 **ZAP and KHNYN iCLIP**

740 Cells were infected at MOI=3 and media was replaced 18 h post-infection with DMEM
741 supplemented with 2% fetal bovine serum. At 48 hours post-infection, cells were washed
742 with ice-cold PBS, irradiated once with 150 mJ/cm2 in a Stratalinker 2400 at 254 nm,
743 harvested by scraping in PBS, pelleted by centrifugation then resuspended in lysis buffer
744 (50 mM Tris-HCl, pH 7.4; 100 mM NaCl; 1% Igepal CA-630; 0.1% SDS; 0.5% sodium
745 deoxycholate; protease inhibitor) and stored at -80°C until use.

746

747 Individual cross-linking and immunoprecipitation (iCLIP) was performed according to the
748 previously published protocol[117], with the following details. For ZAP iCLIP, 4 µg of anti-
749 ZAP antibody (GeneTex, GTX120134) was used for immunoprecipitation per sample. For
750 the KHNYN KO, TRIM25 KO and ZAP-L KO samples, the membrane was cut above 110
751 kDa. In the ZAP-S KO experiments, the membrane was cut from 130 kDa upwards. For
752 KHNYN-GFP iCLIP, 4 µg anti-GFP antibody (Roche, ref. 11814460001) was used for

753 immunoprecipitation per sample. The membrane was cut from 130 kDa upwards. RNA-
754 seq libraries were sequenced by Novogene as paired-end 150 bp reads on Illumina
755 Novaseq 6000. Each iCLIP experiment was performed with three biological replicates.
756
757 **iCLIP data processing**
758 Reads were mapped to the human GRCh38.p13 genome build with GENCODE v38
759 annotation. The HIV-WT or HIV-CpG, genome and annotation were merged with the
760 human genome build and annotation files. Biological replicates were first analyzed
761 individually to assess variability (standard deviation), after which the reads were pooled
762 for all subsequent analyses. Pair-end reads were pre-processed using a custom script
763 written in Bash. Briefly, the unique molecular identifiers (UMIs) were extracted using
764 *UMI-tools extract*[118] (https://github.com/CGATOxford/UMI-tools,*--extract-*
765 *method=regex*) and the paired-end reads merged with *BBTools' BBMerge*[119]
766 (https://sourceforge.net/projects/bbmap/, *mininsert=0, minoverlap=5*). The processed
767 reads were analyzed according to the standardized iCLIP workflow with the *nf-*
768 *core/clipseq v1.0.0* pipeline[120,121] (https://doi.org/10.5281/zenodo.4723017), which was
769 run with *Nextflow v22.10.0*[122] and the following parameters: *--deduplicate true, --*
770 *smrna_org human, --peakcaller paraclu*[123]. In addition, the crosslink BED files generated
771 during the iCLIP analysis were used to call peaks on the HIV-1 genome with *Clippy v1.5.0*
772 tool (https://github.com/ulelab/clippy). The following parameters were used: *--*
773 *window_size 100, --min_prom_adjust 1, --min_height_adjust 1.5, --min_gene_counts 20,*
774 *--min_peak_counts 5.*
775

776 To account for the variability in library size and RNA abundance across experiments, the
777 crosslink signal was normalized in two steps. First, crosslink counts were scaled to
778 counts per million (CPM) using the *clipplotr v1.0.0* command-line tool[124]
779 (https://github.com/ulelab/clipplotr) to adjust for differences in library size. Second, to
780 control for variations in HIV-1 or cellular RNA abundance between samples, CPM-
781 normalized crosslink counts were further adjusted using mean HIV-1 or specific cellular
782 RNA abundance values, calculated from the DESeq2 normalized RNA-seq data across
783 all three biological replicates. The standard error of the mean, shown as the error band
784 on the iCLIP plots, was calculated from the standard deviation of three biological
785 replicates. The data was smoothed using a rolling mean of 100.
786
787 Clippy (https://github.com/ulelab/clippy) was used for peak calling with rollmean100,
788 minHeightAdjust1.5, minPromAdjust1, minGeneCount20, peakWidth0.9, and ≥ 0.25
789 crosslinks/nucleotide. For quantification of signal with specified peaks for HIV-WT or
790 HIV-CpG in Figure S1H-I, the normalized crosslink data was summed for the peaks
791 defined by Clippy for HIV-CpG in HEK293T cells (Peak 1 = nt 304-557, Peak 2 = nt 5650-
792 6438 and Peak 3 = nt 7631-8443). For Figure S6C, the Clippy peaks for HIV-CpG in HeLa
793 CRISPR control cells (Peak 1 = nt 258-535, Peak 2 = nt 5531-6497, Peak 3 = nt 7615-8454)
794 were used to quantify the normalized crosslink data.
795
796 **RNA-seq**
797 RNA was extracted using the Direct-zol RNA Miniprep Plus Kit (Zymo Pure) from cells
798 grown and infected in the same conditions as the iCLIP experiments. Poly(A)+ RNA library
799 preparation and sequencing were performed by GENEWIZ. Sequencing reads were

800 processed using the *nf-core/rnaseq v3.17.0* pipeline[120]
801 (https://doi.org/10.5281/zenodo.13986791) run on *Nextflow v24.04.2*[122] with default
802 parameters. Differentially expressed genes were identified with DESeq2 using the *nf-*
803 *core/differentialabundance v1.2.0* pipeline (https://doi.org/10.5281/zenodo.7846648).
804 To account for transcript length bias, the analysis utilized the raw gene count matrix
805 (salmon.merged.gene_counts.tsv) and transcript length matrix
806 (salmon.merged.gene_lengths.tsv) generated by the *nf-core/rnaseq* pipeline. The
807 pipeline was run with *Nextflow v24.04.2*[122] using default settings. Differentially expressed
808 genes were defined as adjusted p <0.05 and a basemean >500. In addition, ZAP-L
809 regulated genes were defined by log2FC ZAP-L KO / HEK293T cells >0.5 and log2FC ZAP-
810 L KO / ZAP-S KO cells >0.5. ZAP-S regulated genes were defined by log2FC ZAP-S KO /
811 HEK293T cells >0.5 and log2FC ZAP-S KO / ZAP-L KO cells >0.5. ZAP, TRIM25 and KHNYN
812 co-upregulated genes were defined by basemean >500, adjusted p <0.05 and log2FC >
813 0. SignalP 6.0[125] was used to determine if any transcript encoded by ZAP-L or ZAP-S
814 regulated genes in the GENCODE human basic gene annotation CHR was predicted to
815 encode a signal peptide. The presence of transmembrane domains in specific genes was
816 determined using information in the Localization section of GeneCards[126].
817
818 Gene set enrichment analysis (GSEA) was performed using the R package clusterProfiler
819 v4.12.6[127] and human gene sets from the 50 Hallmark pathways obtained using the
820 package msigdbr v7.5.1 (https://CRAN.R-project.org/package=msigdbr). GO
821 enrichment analysis was performed using the DAVID Functional Annotation Tool with
822 Gene Ontology Biological Process, Cellular Component, and Molecular Function Direct
823 terms. The background included all genes with baseMean >500 in HEK293T CRISPR or

824 HeLa CRISPR RNA-seq datasets. Only annotation terms with more than five genes were
825 considered, and significant terms were defined as those with FDR <0.05. Gene
826 expression relationships between different sample sets were analyzed and visualized
827 using the R packages VennDiagram v1.7.3[128] and eulerr v7.0.2 (https://CRAN.R-
828 project.org/package=eulerr). The packages ggplot2 v3.5.1
829 (https://ggplot2.tidyverse.org) and pheatmap v1.0.12
830 (https://github.com/raivokolde/pheatmap) were used to create heat maps of gene
831 expression.
832
833 **5' and 3' RACE-seq**
834 Total RNA was extracted using the Direct-zol RNA Miniprep Plus Kit. The 5' RACE was
835 performed from 1 µg total RNA using the SMARTer RACE 5'/3' Kit according to the
836 manufacturer's instructions. To make cleaved RNA compatible with the 3' RACE cDNA
837 synthesis step, the total RNA was poly(A) tailed using *E. coli* Poly(A) polymerase (NEB)
838 and then purified with the Monarch Spin RNA Cleanup Kit (NEB). The 3' RACE was
839 performed from 500 ng purified poly(A) tailed RNA using the SMARTer RACE 5'/3' Kit
840 according to the manufacturer's instructions. The HIV specific primers used for 5' and 3'
841 RACE are reported in the STAR methods table. RACE sequencing libraries were prepared
842 using the Native Barcoding Kit 24 V14 (Oxford Nanopore Technologies). Sequencing of 5'
843 RACE product libraries was performed on R10.4.1 flowcells (FLO-MIN114, Oxford
844 Nanopore, UK). 3' RACE sequencing libraries were sequenced on PromethION with
845 R10.4.1 flowcells.
846

847 For the 5' RACE-seq, basecalling of *FAST5* files for the first replicate was completed using
848 *guppy_basecaller* (v6.4.6). Dorado (v0.5.1) was used to basecall *POD5* files generated
849 from 5' RACE-seq replicates 2 and 3 as well as the 3' RACE-seq replicates. Reads were
850 basecalled and demultiplexed using the Super High Accuracy (SUP) model (v4.3.0).
851 Additional command-line arguments were implemented to ensure that only reads with
852 identical nanopore barcodes at both ends were considered, as well as excluding any
853 reads containing barcodes in the middle. Bash scripts submitted to KCL's CREATE HPC
854 for basecalling are available on Github (5' RACE-seq: https://github.com/Tycour/HIV1-
855 ZAP_RACEseq; 3' RACE-seq: https://github.com/GregaGD/ZAP_HIV-1_3-prime_RACE-
856 seq), along with the bash scripts and custom Python and R scripts used in the
857 downstream analysis.
858
859 Following basecalling, the FASTQ files were filtered with *NanoFilt v2.8.0*[129] to eliminate
860 low-quality reads and retain reads with an average quality score > Q20. The quality
861 metrics of the filtered reads were evaluated using *NanoPlot v1.42.0*[129]. A custom Python
862 script was implemented to identify and retain reads containing primer sequences at both
863 ends that were used in the RACE reaction. For the 5' RACE reaction, the 5' primer was
864 CTCACTATAGGGCAAGCAGTGGTATCAACGCAGAGTACATGGG and the 3' primer was
865 CCAGCAGCAGATGGGGTGGGAGCAGTAT. For the 3' RACE reaction, the 5' primer was
866 TGGTGGGCGGGGATCAAGCAGGAATTTGGC and the 3' primer was
867 GTACTCTGCGTTGATACCACTGCTTGCCCTATAGTGAG. Reads without internal primer
868 sequences were filtered out to ensure specificity in the downstream analysis.
869

870 Based on the infection conditions, the processed reads were aligned to either the HIV-
871 WT or the HIV-CpG reference genome using *Minimap2*[130,131] *v2.17-r941*, with the splice-
872 aware argument (*--splice*). The alignment files in SAM format were converted to a sorted
873 and indexed BAM format using *samtools (v1.10 or* v1.19). Each read was oriented to the
874 leading or lagging strand using a custom Python script to facilitate downstream
875 processing.
876
877 *Bedtools* (v2.31.1) converted the *BAM* file containing deduplicated reads to *BED* format.
878 For the 5' RACE-seq, an *awk* (v20200816) command was employed to extract the 5' start
879 positions for reads. These positions were then analyzed using a custom script that maps
880 and plots the distribution of read starts along the reference genome. To examine the
881 cleavage sites and detect non-templated nucleotides for the 3' RACE-seq, the alignment
882 files in BAM format were analyzed using a custom R script. Using the *GenomicAlignments*
883 (Lawrence et al., 2013) and *Biostrings* (https://bioconductor.org/packages/Biostrings)
884 packages, the final mapped position of the read was determined by parsing the CIGAR
885 string. Specifically, the last mapped segment was extracted from the CIGAR string and
886 the corresponding 3' end nucleotide position was recorded. This was used in later steps
887 to determine if any nucleotides beyond the mapped part of the read were non-templated.
888
889 Similarly, the *GenomicAlignments*[132] and *Biostrings*
890 (https://bioconductor.org/packages/Biostrings) packages were used to identify
891 stretches of poly(A) nucleotides added during the 3' RACE protocol. The 3' end soft-
892 clipped segment of the read was extracted based on the CIGAR string and analyzed to
893 detect poly(A) segments of at least 15 consecutive adenosines, allowing up to two

mismatches. The position of the poly(A) start in the read sequence was recorded and only reads with recognized poly(A) segments were selected for downstream analysis. The non-templated nucleotides were defined as the sequence between the final mapped position and the start of the poly(A) sequence in each read. The length distribution and nucleotide composition of these regions were analyzed, and the length distribution was visualized with bar charts, while the nucleotide composition per sequence length was visualized with stacked bar charts. The package *ggplot2 v3.5.1* (https://ggplot2.tidyverse.org) was used to generate all charts.

Statistics

Unless otherwise stated, data are represented as mean ± standard deviation and statistical significance was determined by one-way ANOVA or unpaired t test from log-transformed data using GraphPad Prism10 (GraphPad Software Inc.). Significance was ascribed to p values < 0.05 compared to control conditions.

RESOURCE AVAILABILITY

Lead Contact

Additional information and resource requests will be fulfilled by the lead contact, Chad M. Swanson (chad.swanson@kcl.ac.uk).

Materials availability

No new reagents were generated in this study.

Data and code availability

- The poly(A) RNA-seq, iCLIP-seq and RACE-seq data reported in this paper are available at ArrayExpress (E-MTAB-15071, E-MTAB-15072, E-MTAB-15077, E-MTAB-15065, E-MTAB-15056, E-MTAB-15061, E-MTAB-15060, E-MTAB-15095, E-MTAB-15064, E-MTAB-15097). These data are publicly available as of the date of publication.
- Custom scripts for the 5' and 3' RACE analysis are available at https://github.com/Tycour/HIV1-ZAP_RACEseq and https://github.com/GregaGD/ZAP_HIV-1_3-prime_RACE-seq. Other custom analysis scripts are available upon request.
- Any additional information required to reanalyse the data reported in this paper is available from the lead contact upon request.

AUTHOR CONTRIBUTIONS

Conceptualization: C.M.S, S.J.D.N, J.U; Software: A.M.C.; Formal analysis: C.B., G.G.D., M.J.L, R.P.G, T.C., P.K., H.W., P.H., H.M., A.M.C., Investigation: C.B., G.G.D., M.J.L., R.P.G, P.K., H.W.; Writing - Original Draft: C.M.S, C.B., G.G.D., Writing - Review & Editing: all authors; Visualization: C.B., G.G.D, M.J.L, R.P.G., P.K., T.C.; Supervision: J.U., S.J.D.N, C.M.S.; Funding acquisition: M.P., J.U., S.J.D.N., C.M.S.

DECLARATION OF INTERESTS

The authors declare no competing interests.

ACKNOWLEDGEMENTS

941 We thank members of the Ule, Neil and Swanson laboratories for helpful discussions.
942 The following reagents were obtained through the NIH AIDS Research and Reference
943 Reagent Program, Division of AIDS, NIAID, NIH: TZM-bl from Dr. John C. Kappes, Dr.
944 Xiaoyun Wu and Tranzyme Inc; HIV-1 p24 Hybridoma (183-H12-5C) from Dr. Bruce
945 Chesebro. The Antiserum to HIV-1 gp120 #20 (ARP421) was obtained from the NIBSC
946 Centre for AIDS Reagents. We thank Xavier Roca for the ZAP-L and ZAP-S knockout cells.
947 We also thank Rebecca Sumner for the AP-1 reporter plasmid. We gratefully acknowledge
948 the support of King's Genomics, Social Genetic & Development Psychiatry Centre,
949 Institute of Psychiatry, Psychology & Neuroscience, King's College London for the Oxford
950 Nanopore Technologies PromethION sequencing and the HPC CREATE at King's College
951 London. We also thank the Nikon Imaging Centre at Kings College London for help with
952 light microscopy. These studies were funded by Medical Research Council grants
953 MR/S000844/1 and MR/W018519/1 to SJDN and CMS, Wellcome Early Career Award
954 (225081/Z/22/Z) to AMC, Sir Henry Dale Fellowship from the Wellcome Trust and the
955 Royal Society (218537/Z/19/Z) to HEM, Wellcome Trust Senior Research Fellowship
956 (WT098049AIA) to SJDN, the European Research Council (ERC) under the European
957 Union's Horizon 2020 research and innovation programme (grant agreement No 835300)
958 to JU, and Slovenian Research and Innovation Agency ARIS grant P3-00083 to MP and
959 GGD. The Slovenian Research Agency financially supported GGD through the Young
960 Researcher Training Program for four years (2021–2025; contract number 802-7/2021-1).
961

962 **REFERENCES**

963 1. Chan, C.P., and Jin, D.Y. (2022). Cytoplasmic RNA sensors and their interplay with
964 RNA-binding partners in innate antiviral response: theme and variations. RNA *28*,
965 449–477. 10.1261/rna.079016.121.

2. Yang, E., and Li, M.M.H. (2020). All About the RNA: Interferon-Stimulated Genes That Interfere With Viral RNA Processes. Front Immunol *11*, 605024. 10.3389/fimmu.2020.605024.
3. Gao, G., Guo, X., and Goff, S.P. (2002). Inhibition of retroviral RNA production by ZAP, a CCCH-type zinc finger protein. Science *297*, 1703–1706. 10.1126/science.1074276.
4. Ficarelli, M., Neil, S.J.D., and Swanson, C.M. (2021). Targeted Restriction of Viral Gene Expression and Replication by the ZAP Antiviral System. Annu Rev Virol *8*, 265–283. 10.1146/annurev-virology-091919-104213.
5. Shao, R., Visser, I., Fros, J.J., and Yin, X. (2024). Versatility of the Zinc-Finger Antiviral Protein (ZAP) As a Modulator of Viral Infections. Int J Biol Sci *20*, 4585–4600. 10.7150/ijbs.98029.
6. Bick, M.J., Carroll, J.W., Gao, G., Goff, S.P., Rice, C.M., and MacDonald, M.R. (2003). Expression of the zinc-finger antiviral protein inhibits alphavirus replication. J Virol *77*, 11555–11562. 10.1128/jvi.77.21.11555-11562.2003.
7. Zhu, Y., Wang, X., Goff, S.P., and Gao, G. (2012). Translational repression precedes and is required for ZAP-mediated mRNA decay. EMBO J *31*, 4236–4246. 10.1038/emboj.2012.271.
8. Zimmer, M.M., Kibe, A., Rand, U., Pekarek, L., Ye, L., Buck, S., Smyth, R.P., Cicin-Sain, L., and Caliskan, N. (2021). The short isoform of the host antiviral protein ZAP acts as an inhibitor of SARS-CoV-2 programmed ribosomal frameshifting. Nature communications *12*, 7193. 10.1038/s41467-021-27431-0.
9. Takata, M.A., Goncalves-Carneiro, D., Zang, T.M., Soll, S.J., York, A., Blanco-Melo, D., and Bieniasz, P.D. (2017). CG dinucleotide suppression enables antiviral defence targeting non-self RNA. Nature *550*, 124–127. 10.1038/nature24039.
10. Meagher, J.L., Takata, M., Goncalves-Carneiro, D., Keane, S.C., Rebendenne, A., Ong, H., Orr, V.K., MacDonald, M.R., Stuckey, J.A., Bieniasz, P.D., and Smith, J.L. (2019). Structure of the zinc-finger antiviral protein in complex with RNA reveals a mechanism for selective targeting of CG-rich viral sequences. Proc Natl Acad Sci U S A *116*, 24303–24309. 10.1073/pnas.1913232116.
11. Odon, V., Fros, J.J., Goonawardane, N., Dietrich, I., Ibrahim, A., Alshaikhahmed, K., Nguyen, D., and Simmonds, P. (2019). The role of ZAP and OAS3/RNAseL pathways in the attenuation of an RNA virus with elevated frequencies of CpG and UpA dinucleotides. Nucleic Acids Res *47*, 8061–8083. 10.1093/nar/gkz581.
12. Luo, X., Wang, X., Gao, Y., Zhu, J., Liu, S., Gao, G., and Gao, P. (2020). Molecular Mechanism of RNA Recognition by Zinc-Finger Antiviral Protein. Cell reports *30*, 46–52 e44. 10.1016/j.celrep.2019.11.116.
13. Fros, J.J., Visser, I., Tang, B., Yan, K., Nakayama, E., Visser, T.M., Koenraadt, C.J.M., van Oers, M.M., Pijlman, G.P., Suhrbier, A., and Simmonds, P. (2021). The dinucleotide composition of the Zika virus genome is shaped by conflicting evolutionary pressures in mammalian hosts and mosquito vectors. PLoS Biol *19*, e3001201. 10.1371/journal.pbio.3001201.
14. Sharp, C.P., Thompson, B.H., Nash, T.J., Diebold, O., Pinto, R.M., Thorley, L., Lin, Y.T., Sives, S., Wise, H., Clohisey Hendry, S., et al. (2023). CpG dinucleotide enrichment in the influenza A virus genome as a live attenuated vaccine

development strategy. PLoS Pathog *19*, e1011357. 10.1371/journal.ppat.1011357.

15. Le, N.P.K., Singh, P.P., Trus, I., and Karniychuk, U. (2025). West Nile virus vaccine candidates attenuated by dinucleotide enrichment are immunogenic and protective against lethal infection. PLoS Pathog *21*, e1013560. 10.1371/journal.ppat.1013560.
16. Goonawardane, N., Nguyen, D., and Simmonds, P. (2021). Association of Zinc Finger Antiviral Protein Binding to Viral Genomic RNA with Attenuation of Replication of Echovirus 7. mSphere *6*, e01138–01120. 10.1128/mSphere.01138-20.
17. Goncalves-Carneiro, D., Mastrocola, E., Lei, X., DaSilva, J., Chan, Y.F., and Bieniasz, P.D. (2022). Rational attenuation of RNA viruses with zinc finger antiviral protein. Nat Microbiol *7*, 1558–1567. 10.1038/s41564-022-01223-8.
18. Karlin, S., Doerfler, W., and Cardon, L.R. (1994). Why is CpG suppressed in the genomes of virtually all small eukaryotic viruses but not in those of large eukaryotic viruses? J Virol *68*, 2889–2897. 10.1128/JVI.68.5.2889-2897.1994.
19. Guo, X., Carroll, J.W., Macdonald, M.R., Goff, S.P., and Gao, G. (2004). The zinc finger antiviral protein directly binds to specific viral mRNAs through the CCCH zinc finger motifs. J Virol *78*, 12781–12787. 10.1128/JVI.78.23.12781-12787.2004.
20. Chen, S., Xu, Y., Zhang, K., Wang, X., Sun, J., Gao, G., and Liu, Y. (2012). Structure of N-terminal domain of ZAP indicates how a zinc-finger protein recognizes complex RNA. Nat Struct Mol Biol *19*, 430–435. 10.1038/nsmb.2243.
21. Ficarelli, M., Antzin-Anduetza, I., Hugh-White, R., Firth, A.E., Sertkaya, H., Wilson, H., Neil, S.J.D., Schulz, R., and Swanson, C.M. (2020). CpG Dinucleotides Inhibit HIV-1 Replication through Zinc Finger Antiviral Protein (ZAP)-Dependent and -Independent Mechanisms. J Virol *94*, e01337–01319. 10.1128/JVI.01337-19.
22. Groenke, N., Trimpert, J., Merz, S., Conradie, A.M., Wyler, E., Zhang, H., Hazapis, O.G., Rausch, S., Landthaler, M., Osterrieder, N., and Kunec, D. (2020). Mechanism of Virus Attenuation by Codon Pair Deoptimization. Cell reports *31*, 107586. 10.1016/j.celrep.2020.107586.
23. Nguyen, L.P., Aldana, K.S., Yang, E., Yao, Z., and Li, M.M.H. (2023). Alphavirus Evasion of Zinc Finger Antiviral Protein (ZAP) Correlates with CpG Suppression in a Specific Viral nsP2 Gene Sequence. Viruses *15*. 10.3390/v15040830.
24. Kmiec, D., Nchioua, R., Sherrill-Mix, S., Sturzel, C.M., Heusinger, E., Braun, E., Gondim, M.V.P., Hotter, D., Sparrer, K.M.J., Hahn, B.H., et al. (2020). CpG Frequency in the 5' Third of the env Gene Determines Sensitivity of Primary HIV-1 Strains to the Zinc-Finger Antiviral Protein. mBio *11*, e02903–02919. 10.1128/mBio.02903-19.
25. Sertkaya, H., Hidalgo, L., Ficarelli, M., Kmiec, D., Signell, A.W., Ali, S., Parker, H., Wilson, H., Neil, S.J.D., Malim, M.H., et al. (2021). Minimal impact of ZAP on lentiviral vector production and transduction efficiency. Mol Ther Methods Clin Dev *23*, 147–157. 10.1016/j.omtm.2021.08.008.
26. Todorova, T., Bock, F.J., and Chang, P. (2014). PARP13 regulates cellular mRNA post-transcriptionally and functions as a pro-apoptotic factor by destabilizing TRAILR4 transcript. Nature communications *5*, 5362. 10.1038/ncomms6362.

27. Ly, P.T., Xu, S., Wirawan, M., Luo, D., and Roca, X. (2022). ZAP isoforms regulate unfolded protein response and epithelial- mesenchymal transition. Proc Natl Acad Sci U S A *119*, e2121453119. 10.1073/pnas.2121453119.
28. Goncalves-Carneiro, D., Mastrocola, E., Lei, X., and Bieniasz, P.D. (2025). Modulation of host gene expression by the zinc finger antiviral protein. Proc Natl Acad Sci U S A *122*, e2420819122. 10.1073/pnas.2420819122.
29. Busa, V.F., Ando, Y., Aigner, S., Yee, B.A., Yeo, G.W., and Leung, A.K.L. (2024). Transcriptome regulation by PARP13 in basal and antiviral states in human cells. iScience *27*, 109251. 10.1016/j.isci.2024.109251.
30. Cooper, D.N., and Gerber-Huber, S. (1985). DNA methylation and CpG suppression. Cell Differ *17*, 199–205. 10.1016/0045-6039(85)90488-9.
31. Shaw, A.E., Rihn, S.J., Mollentze, N., Wickenhagen, A., Stewart, D.G., Orton, R.J., Kuchi, S., Bakshi, S., Collados, M.R., Turnbull, M.L., et al. (2021). The antiviral state has shaped the CpG composition of the vertebrate interferome to avoid self-targeting. PLoS Biol *19*, e3001352. 10.1371/journal.pbio.3001352.
32. Nchioua, R., Kmiec, D., Krchlikova, V., Mattes, S., Noettger, S., Bibollet-Ruche, F., Russell, R.M., Sparrer, K.M.J., Charpentier, T., Tardy, F., et al. (2025). Host ZAP activity correlates with the levels of CpG suppression in primate lentiviruses. Proc Natl Acad Sci U S A *122*, e2419489122. 10.1073/pnas.2419489122.
33. Guo, X., Ma, J., Sun, J., and Gao, G. (2007). The zinc-finger antiviral protein recruits the RNA processing exosome to degrade the target mRNA. Proc Natl Acad Sci U S A *104*, 151–156. 10.1073/pnas.0607063104.
34. Zhu, Y., Chen, G., Lv, F., Wang, X., Ji, X., Xu, Y., Sun, J., Wu, L., Zheng, Y.T., and Gao, G. (2011). Zinc-finger antiviral protein inhibits HIV-1 infection by selectively targeting multiply spliced viral mRNAs for degradation. Proc Natl Acad Sci U S A *108*, 15834–15839. 10.1073/pnas.1101676108.
35. Chen, G., Guo, X., Lv, F., Xu, Y., and Gao, G. (2008). p72 DEAD box RNA helicase is required for optimal function of the zinc-finger antiviral protein. Proc Natl Acad Sci U S A *105*, 4352–4357. 10.1073/pnas.0712276105.
36. Lee, H., Komano, J., Saitoh, Y., Yamaoka, S., Kozaki, T., Misawa, T., Takahama, M., Satoh, T., Takeuchi, O., Yamamoto, N., et al. (2013). Zinc-finger antiviral protein mediates retinoic acid inducible gene I-like receptor-independent antiviral response to murine leukemia virus. Proc Natl Acad Sci U S A *110*, 12379–12384. 10.1073/pnas.1310604110.
37. Ye, P., Liu, S., Zhu, Y., Chen, G., and Gao, G. (2010). DEXH-Box protein DHX30 is required for optimal function of the zinc-finger antiviral protein. Protein Cell *1*, 956–964. 10.1007/s13238-010-0117-8.
38. Li, M.M., Lau, Z., Cheung, P., Aguilar, E.G., Schneider, W.M., Bozzacco, L., Molina, H., Buehler, E., Takaoka, A., Rice, C.M., et al. (2017). TRIM25 Enhances the Antiviral Action of Zinc-Finger Antiviral Protein (ZAP). PLoS Pathog *13*, e1006145. 10.1371/journal.ppat.1006145.
39. Zheng, X., Wang, X., Tu, F., Wang, Q., Fan, Z., and Gao, G. (2017). TRIM25 Is Required for the Antiviral Activity of Zinc Finger Antiviral Protein. J Virol *91*, e00088–00017. 10.1128/JVI.00088-17.
40. Ficarelli, M., Wilson, H., Pedro Galao, R., Mazzon, M., Antzin-Anduetza, I., Marsh, M., Neil, S.J., and Swanson, C.M. (2019). KHNYN is essential for the zinc finger

antiviral protein (ZAP) to restrict HIV-1 containing clustered CpG dinucleotides. Elife *8*, e46767. 10.7554/eLife.46767.

41. Bohn, J.A., Meagher, J.L., Takata, M.A., Goncalves-Carneiro, D., Yeoh, Z.C., Ohi, M.D., Smith, J.L., and Bieniasz, P.D. (2024). Functional anatomy of zinc finger antiviral protein complexes. Nature communications *15*, 10834. 10.1038/s41467-024-55192-z.

42. Yeoh, Z.C., Meagher, J.L., Kang, C.Y., Bieniasz, P.D., Smith, J.L., and Ohi, M.D. (2024). A minimal complex of KHNYN and zinc-finger antiviral protein binds and degrades single-stranded RNA. Proc Natl Acad Sci U S A *121*, e2415048121. 10.1073/pnas.2415048121.

43. OhAinle, M., Helms, L., Vermeire, J., Roesch, F., Humes, D., Basom, R., Delrow, J.J., Overbaugh, J., and Emerman, M. (2018). A virus-packageable CRISPR screen identifies host factors mediating interferon inhibition of HIV. Elife *7*, e39823. 10.7554/eLife.39823.

44. Youle, R.L., Lista, M.J., Bouton, C., Kunzelmann, S., Wilson, H., Cottee, M.A., Purkiss, A.G., Morris, E.R., Neil, S.J.D., Taylor, I.A., and Swanson, C.M. (2025). Structural and functional characterization of the extended-diKH domain from the antiviral endoribonuclease KHNYN. J Biol Chem, 108336. 10.1016/j.jbc.2025.108336.

45. Kerns, J.A., Emerman, M., and Malik, H.S. (2008). Positive selection and increased antiviral activity associated with the PARP-containing isoform of human zinc-finger antiviral protein. PLoS genetics *4*, e21. 10.1371/journal.pgen.0040021.

46. Li, M.M.H., Aguilar, E.G., Michailidis, E., Pabon, J., Park, P., Wu, X., de Jong, Y.P., Schneider, W.M., Molina, H., Rice, C.M., and MacDonald, M.R. (2019). Characterization of Novel Splice Variants of Zinc Finger Antiviral Protein (ZAP). J Virol *93*, e00715–00719. 10.1128/JVI.00715-19.

47. Hayakawa, S., Shiratori, S., Yamato, H., Kameyama, T., Kitatsuji, C., Kashigi, F., Goto, S., Kameoka, S., Fujikura, D., Yamada, T., et al. (2011). ZAPS is a potent stimulator of signaling mediated by the RNA helicase RIG-I during antiviral responses. Nat Immunol *12*, 37–44. 10.1038/ni.1963.

48. Nchioua, R., Kmiec, D., Muller, J.A., Conzelmann, C., Gross, R., Swanson, C.M., Neil, S.J.D., Stenger, S., Sauter, D., Munch, J., et al. (2020). SARS-CoV-2 Is Restricted by Zinc Finger Antiviral Protein despite Preadaptation to the Low-CpG Environment in Humans. mBio *11*, e01930–01920. 10.1128/mBio.01930-20.

49. Xue, G., Braczyk, K., Goncalves-Carneiro, D., Dawidziak, D.M., Sanchez, K., Ong, H., Wan, Y., Zadrozny, K.K., Ganser-Pornillos, B.K., Bieniasz, P.D., and Pornillos, O. (2022). Poly(ADP-ribose) potentiates ZAP antiviral activity. PLoS Pathog *18*, e1009202. 10.1371/journal.ppat.1009202.

50. Kuttiyatveetil, J.R.A., Soufari, H., Dasovich, M., Uribe, I.R., Mirhasan, M., Cheng, S.J., Leung, A.K.L., and Pascal, J.M. (2022). Crystal structures and functional analysis of the ZnF5-WWE1-WWE2 region of PARP13/ZAP define a distinctive mode of engaging poly(ADP-ribose). Cell reports *41*, 111529. 10.1016/j.celrep.2022.111529.

51. Charron, G., Li, M.M., MacDonald, M.R., and Hang, H.C. (2013). Prenylome profiling reveals S-farnesylation is crucial for membrane targeting and antiviral

activity of ZAP long-isoform. Proc Natl Acad Sci U S A *110*, 11085–11090. 10.1073/pnas.1302564110.

52. Schwerk, J., Soveg, F.W., Ryan, A.P., Thomas, K.R., Hatfield, L.D., Ozarkar, S., Forero, A., Kell, A.M., Roby, J.A., So, L., et al. (2019). RNA-binding protein isoforms ZAP-S and ZAP-L have distinct antiviral and immune resolution functions. Nat Immunol *20*, 1610–1620. 10.1038/s41590-019-0527-6.

53. Kmiec, D., Lista, M.J., Ficarelli, M., Swanson, C.M., and Neil, S.J.D. (2021). S-farnesylation is essential for antiviral activity of the long ZAP isoform against RNA viruses with diverse replication strategies. PLoS Pathog *17*, e1009726. 10.1371/journal.ppat.1009726.

54. Kim, M., Pyo, Y., Hyun, S.I., Jeong, M., Choi, Y., and Kim, V.N. (2025). Exogenous RNA surveillance by proton-sensing TRIM25. Science *388*, eads4539. 10.1126/science.ads4539.

55. Lin, Y., Zhang, H., Liang, J., Li, K., Zhu, W., Fu, L., Wang, F., Zheng, X., Shi, H., Wu, S., et al. (2014). Identification and characterization of alphavirus M1 as a selective oncolytic virus targeting ZAP-defective human cancers. Proc Natl Acad Sci U S A *111*, E4504–4512. 10.1073/pnas.1408759111.

56. Kypr, J., Mrazek, J., and Reich, J. (1989). Nucleotide composition bias and CpG dinucleotide content in the genomes of HIV and HTLV 1/2. Biochim Biophys Acta *1009*, 280–282. 10.1016/0167-4781(89)90114-0.

57. Shpaer, E.G., and Mullins, J.I. (1990). Selection against CpG dinucleotides in lentiviral genes: a possible role of methylation in regulation of viral expression. Nucleic Acids Res *18*, 5793–5797. 10.1093/nar/18.19.5793.

58. Wasson, M.K., Borkakoti, J., Kumar, A., Biswas, B., and Vivekanandan, P. (2017). The CpG dinucleotide content of the HIV-1 envelope gene may predict disease progression. Sci Rep *7*, 8162. 10.1038/s41598-017-08716-1.

59. Theys, K., Feder, A.F., Gelbart, M., Hartl, M., Stern, A., and Pennings, P.S. (2018). Within-patient mutation frequencies reveal fitness costs of CpG dinucleotides and drastic amino acid changes in HIV. PLoS genetics *14*, e1007420. 10.1371/journal.pgen.1007420.

60. Goncalves-Carneiro, D., Takata, M.A., Ong, H., Shilton, A., and Bieniasz, P.D. (2021). Origin and evolution of the zinc finger antiviral protein. PLoS Pathog *17*, e1009545. 10.1371/journal.ppat.1009545.

61. Lista, M.J., Ficarelli, M., Wilson, H., Kmiec, D., Youle, R.L., Wanford, J., Winstone, H., Odendall, C., Taylor, I.A., Neil, S.J.D., and Swanson, C.M. (2023). A Nuclear Export Signal in KHNYN Required for Its Antiviral Activity Evolved as ZAP Emerged in Tetrapods. J Virol *97*, e0087222. 10.1128/jvi.00872-22.

62. Konig, J., Zarnack, K., Rot, G., Curk, T., Kayikci, M., Zupan, B., Turner, D.J., Luscombe, N.M., and Ule, J. (2010). iCLIP reveals the function of hnRNP particles in splicing at individual nucleotide resolution. Nat Struct Mol Biol *17*, 909–915. 10.1038/nsmb.1838.

63. Keane, S.C., and Summers, M.F. (2016). NMR Studies of the Structure and Function of the HIV-1 5'-Leader. Viruses *8*, 338. 10.3390/v8120338.

64. Sertznig, H., Hillebrand, F., Erkelenz, S., Schaal, H., and Widera, M. (2018). Behind the scenes of HIV-1 replication: Alternative splicing as the dependency factor on the quiet. Virology *516*, 176–188. 10.1016/j.virol.2018.01.011.

1196 65. Law, L.M., Albin, O.R., Carroll, J.W., Jones, C.T., Rice, C.M., and Macdonald, M.R.
1197 (2010). Identification of a dominant negative inhibitor of human zinc finger
1198 antiviral protein reveals a functional endogenous pool and critical homotypic
1199 interactions. J Virol *84*, 4504–4512. 10.1128/JVI.02018-09.
1200 66. Hamid, F.M., and Makeyev, E.V. (2016). Exaptive origins of regulated mRNA decay
1201 in eukaryotes. Bioessays *38*, 830–838. 10.1002/bies.201600100.
1202 67. Kuret, K., Amalietti, A.G., Jones, D.M., Capitanchik, C., and Ule, J. (2022).
1203 Positional motif analysis reveals the extent of specificity of protein-RNA
1204 interactions observed by CLIP. Genome Biol *23*, 191. 10.1186/s13059-022-
1205 02755-2.
1206 68. Leung, A.K., Vyas, S., Rood, J.E., Bhutkar, A., Sharp, P.A., and Chang, P. (2011).
1207 Poly(ADP-ribose) regulates stress responses and microRNA activity in the
1208 cytoplasm. Mol Cell *42*, 489–499. 10.1016/j.molcel.2011.04.015.
1209 69. Seo, G.J., Kincaid, R.P., Phanaksri, T., Burke, J.M., Pare, J.M., Cox, J.E., Hsiang,
1210 T.Y., Krug, R.M., and Sullivan, C.S. (2013). Reciprocal inhibition between
1211 intracellular antiviral signaling and the RNAi machinery in mammalian cells. Cell
1212 Host Microbe *14*, 435–445. 10.1016/j.chom.2013.09.002.
1213 70. Simmonds, P., Xia, W., Baillie, J.K., and McKinnon, K. (2013). Modelling
1214 mutational and selection pressures on dinucleotides in eukaryotic phyla--
1215 selection against CpG and UpA in cytoplasmically expressed RNA and in RNA
1216 viruses. BMC genomics *14*, 610. 10.1186/1471-2164-14-610.
1217 71. Gonzalez-Perez, A.C., Stempel, M., Wyler, E., Urban, C., Piras, A., Hennig, T.,
1218 Ganskih, S., Wei, Y., Heim, A., Landthaler, M., et al. (2021). The Zinc Finger
1219 Antiviral Protein ZAP Restricts Human Cytomegalovirus and Selectively Binds
1220 and Destabilizes Viral UL4/UL5 Transcripts. mBio *12*. 10.1128/mBio.02683-20.
1221 72. Lin, Y.T., Chiweshe, S., McCormick, D., Raper, A., Wickenhagen, A., DeFillipis, V.,
1222 Gaunt, E., Simmonds, P., Wilson, S.J., and Grey, F. (2020). Human
1223 cytomegalovirus evades ZAP detection by suppressing CpG dinucleotides in the
1224 major immediate early 1 gene. PLoS Pathog *16*, e1008844.
1225 10.1371/journal.ppat.1008844.
1226 73. Lista, M.J., Witney, A.A., Nichols, J., Davison, A.J., Wilson, H., Latham, K.A.,
1227 Ravenhill, B.J., Nightingale, K., Stanton, R.J., Weekes, M.P., et al. (2023). Strain-
1228 Dependent Restriction of Human Cytomegalovirus by Zinc Finger Antiviral
1229 Proteins. J Virol, e0184622. 10.1128/jvi.01846-22.
1230 74. Galao, R.P., Wilson, H., Schierhorn, K.L., Debeljak, F., Bodmer, B.S., Goldhill, D.,
1231 Hoenen, T., Wilson, S.J., Swanson, C.M., and Neil, S.J.D. (2022). TRIM25 and ZAP
1232 target the Ebola virus ribonucleoprotein complex to mediate interferon-induced
1233 restriction. PLoS Pathog *18*, e1010530. 10.1371/journal.ppat.1010530.
1234 75. Goodier, J.L., Pereira, G.C., Cheung, L.E., Rose, R.J., and Kazazian, H.H., Jr.
1235 (2015). The Broad-Spectrum Antiviral Protein ZAP Restricts Human
1236 Retrotransposition. PLoS genetics *11*, e1005252.
1237 10.1371/journal.pgen.1005252.
1238 76. Youn, J.Y., Dunham, W.H., Hong, S.J., Knight, J.D.R., Bashkurov, M., Chen, G.I.,
1239 Bagci, H., Rathod, B., MacLeod, G., Eng, S.W.M., et al. (2018). High-Density
1240 Proximity Mapping Reveals the Subcellular Organization of mRNA-Associated
1241 Granules and Bodies. Mol Cell *69*, 517–532 e511. 10.1016/j.molcel.2017.12.020.

77. Lau, N.C., Kolkman, A., van Schaik, F.M., Mulder, K.W., Pijnappel, W.W., Heck, A.J., and Timmers, H.T. (2009). Human Ccr4-Not complexes contain variable deadenylase subunits. Biochem J *422*, 443–453. 10.1042/BJ20090500.
78. Yu, S., and Kim, V.N. (2020). A tale of non-canonical tails: gene regulation by post-transcriptional RNA tailing. Nat Rev Mol Cell Biol *21*, 542–556. 10.1038/s41580-020-0246-8.
79. Chang, H.M., Triboulet, R., Thornton, J.E., and Gregory, R.I. (2013). A role for the Perlman syndrome exonuclease Dis3l2 in the Lin28-let-7 pathway. Nature *497*, 244–248. 10.1038/nature12119.
80. Lubas, M., Damgaard, C.K., Tomecki, R., Cysewski, D., Jensen, T.H., and Dziembowski, A. (2013). Exonuclease hDIS3L2 specifies an exosome-independent 3'-5' degradation pathway of human cytoplasmic mRNA. EMBO J *32*, 1855–1868. 10.1038/emboj.2013.135.
81. Malecki, M., Viegas, S.C., Carneiro, T., Golik, P., Dressaire, C., Ferreira, M.G., and Arraiano, C.M. (2013). The exoribonuclease Dis3L2 defines a novel eukaryotic RNA degradation pathway. EMBO J *32*, 1842–1854. 10.1038/emboj.2013.63.
82. Sharp, C.P., Thompson, B.H., Hoque, A.F., Diebold, O., Tesla, B., Kurian, D., Simmonds, P., Digard, P., and Gaunt, E. (2025). Understanding off-target growth defects introduced to influenza A virus by synonymous recoding. RNA *31*, 1557–1574. 10.1261/rna.080675.125.
83. Wang, Y., Ma, T., He, Y., Li, Q., Mai, K., Mo, M., Cao, C., Li, J., Feng, P., Peng, J., et al. (2025). Genome-Wide Codon Reprogramming Enables a Multifactorially Attenuated Influenza Vaccine with Broad Cross-Protection. Adv Sci (Weinh), e16448. 10.1002/advs.202516448.
84. Fazal, F.M., Han, S., Parker, K.R., Kaewsapsak, P., Xu, J., Boettiger, A.N., Chang, H.Y., and Ting, A.Y. (2019). Atlas of Subcellular RNA Localization Revealed by APEX-Seq. Cell *178*, 473–490 e426. 10.1016/j.cell.2019.05.027.
85. Schuhmacher, J.S., Tom Dieck, S., Christoforidis, S., Landerer, C., Davila Gallesio, J., Hersemann, L., Seifert, S., Schafer, R., Giner, A., Toth-Petroczy, A., et al. (2023). The Rab5 effector FERRY links early endosomes with mRNA localization. Mol Cell *83*, 1839–1855 e1813. 10.1016/j.molcel.2023.05.012.
86. Horste, E.L., Fansler, M.M., Cai, T., Chen, X., Mitschka, S., Zhen, G., Lee, F.C.Y., Ule, J., and Mayr, C. (2023). Subcytoplasmic location of translation controls protein output. Mol Cell *83*, 4509–4523 e4511. 10.1016/j.molcel.2023.11.025.
87. Bae, J.W., Kwon, S.C., Na, Y., Kim, V.N., and Kim, J.S. (2020). Chemical RNA digestion enables robust RNA-binding site mapping at single amino acid resolution. Nat Struct Mol Biol *27*, 678–682. 10.1038/s41594-020-0436-2.
88. Todorova, T., Bock, F.J., and Chang, P. (2015). Poly(ADP-ribose) polymerase-13 and RNA regulation in immunity and cancer. Trends in molecular medicine *21*, 373–384. 10.1016/j.molmed.2015.03.002.
89. Shaw, A.E., Hughes, J., Gu, Q., Behdenna, A., Singer, J.B., Dennis, T., Orton, R.J., Varela, M., Gifford, R.J., Wilson, S.J., and Palmarini, M. (2017). Fundamental properties of the mammalian innate immune system revealed by multispecies comparison of type I interferon responses. PLoS Biol *15*, e2004086. 10.1371/journal.pbio.2004086.
90. Zheng, W., Guo, J., Ma, S., Sun, R., Song, Y., Chen, Y., Mao, R., and Fan, Y. (2024). The NEDD4-binding protein N4BP1 degrades mRNA substrates through the

coding sequence independent of nonsense-mediated decay. J Biol Chem *300*, 107954. 10.1016/j.jbc.2024.107954.

91. Tse, K.M., and Takeuchi, O. (2023). Innate immune sensing of pathogens and its post-transcriptional regulations by RNA-binding proteins. Arch Pharm Res *46*, 65–77. 10.1007/s12272-023-01429-2.

92. Youle, R.L., Lista, M.J., Brudenell, E.L., Thompson, B., Bouton, C., Morris, E.R., Neil, S.J.D., Swanson, C.M., and Taylor, I.A. (2025). KHNYN is a manganese-dependent endoribonuclease required for ZAP-mediated antiviral restriction. Nucleic Acids Res *53*. 10.1093/nar/gkaf1360.

93. Wang, C., Guan, Y., Lv, M., Zhang, R., Guo, Z., Wei, X., Du, X., Yang, J., Li, T., Wan, Y., et al. (2018). Manganese Increases the Sensitivity of the cGAS-STING Pathway for Double-Stranded DNA and Is Required for the Host Defense against DNA Viruses. Immunity *48*, 675–687 e677. 10.1016/j.immuni.2018.03.017.

94. Yang, E., Huang, S., Jami-Alahmadi, Y., McInerney, G.M., Wohlschlegel, J.A., and Li, M.M.H. (2022). Elucidation of TRIM25 ubiquitination targets involved in diverse cellular and antiviral processes. PLoS Pathog *18*, e1010743. 10.1371/journal.ppat.1010743.

95. Sanchez, J.G., Chiang, J.J., Sparrer, K.M.J., Alam, S.L., Chi, M., Roganowicz, M.D., Sankaran, B., Gack, M.U., and Pornillos, O. (2016). Mechanism of TRIM25 Catalytic Activation in the Antiviral RIG-I Pathway. Cell reports *16*, 1315–1325. 10.1016/j.celrep.2016.06.070.

96. Choudhury, N.R., Heikel, G., Trubitsyna, M., Kubik, P., Nowak, J.S., Webb, S., Granneman, S., Spanos, C., Rappsilber, J., Castello, A., and Michlewski, G. (2017). RNA-binding activity of TRIM25 is mediated by its PRY/SPRY domain and is required for ubiquitination. BMC Biol *15*, 105. 10.1186/s12915-017-0444-9.

97. Sanchez, J.G., Sparrer, K.M.J., Chiang, C., Reis, R.A., Chiang, J.J., Zurenski, M.A., Wan, Y., Gack, M.U., and Pornillos, O. (2018). TRIM25 Binds RNA to Modulate Cellular Anti-viral Defense. J Mol Biol *430*, 5280–5293. 10.1016/j.jmb.2018.10.003.

98. Alvarez, L., Haubrich, K., Iselin, L., Gillioz, L., Ruscica, V., Lapouge, K., Augsten, S., Huppertz, I., Choudhury, N.R., Simon, B., et al. (2024). The molecular dissection of TRIM25's RNA-binding mechanism provides key insights into its antiviral activity. Nature communications *15*, 8485. 10.1038/s41467-024-52918-x.

99. Choudhury, N.R., Nowak, J.S., Zuo, J., Rappsilber, J., Spoel, S.H., and Michlewski, G. (2014). Trim25 Is an RNA-Specific Activator of Lin28a/TuT4-Mediated Uridylation. Cell reports *9*, 1265–1272. 10.1016/j.celrep.2014.10.017.

100. Kwon, S.C., Yi, H., Eichelbaum, K., Fohr, S., Fischer, B., You, K.T., Castello, A., Krijgsveld, J., Hentze, M.W., and Kim, V.N. (2013). The RNA-binding protein repertoire of embryonic stem cells. Nat Struct Mol Biol *20*, 1122–1130. 10.1038/nsmb.2638.

101. Manokaran, G., Finol, E., Wang, C., Gunaratne, J., Bahl, J., Ong, E.Z., Tan, H.C., Sessions, O.M., Ward, A.M., Gubler, D.J., et al. (2015). Dengue subgenomic RNA binds TRIM25 to inhibit interferon expression for epidemiological fitness. Science *350*, 217–221. 10.1126/science.aab3369.

102. Choudhury, N.R., Trus, I., Heikel, G., Wolczyk, M., Szymanski, J., Bolembach, A., Dos Santos Pinto, R.M., Smith, N., Trubitsyna, M., Gaunt, E., et al. (2022). TRIM25

1336 inhibits influenza A virus infection, destabilizes viral mRNA, but is redundant for
1337 activating the RIG-I pathway. Nucleic Acids Res *50*, 7097–7114.
1338 10.1093/nar/gkac512.
1339 103. Le Pen, J., Jiang, H., Di Domenico, T., Kneuss, E., Kosalka, J., Leung, C., Morgan,
1340 M., Much, C., Rudolph, K.L.M., Enright, A.J., et al. (2018). Terminal
1341 uridylyltransferases target RNA viruses as part of the innate immune system. Nat
1342 Struct Mol Biol *25*, 778–786. 10.1038/s41594-018-0106-9.
1343 104. Huo, Y., Shen, J., Wu, H., Zhang, C., Guo, L., Yang, J., and Li, W. (2016).
1344 Widespread 3'-end uridylation in eukaryotic RNA viruses. Sci Rep *6*, 25454.
1345 10.1038/srep25454.
1346 105. Warkocki, Z., Krawczyk, P.S., Adamska, D., Bijata, K., Garcia-Perez, J.L., and
1347 Dziembowski, A. (2018). Uridylation by TUT4/7 Restricts Retrotransposition of
1348 Human LINE-1s. Cell *174*, 1537–1548 e1529. 10.1016/j.cell.2018.07.022.
1349 106. Meze, K., Axhemi, A., Thomas, D.R., Doymaz, A., and Joshua-Tor, L. (2023). A
1350 shape-shifting nuclease unravels structured RNA. Nat Struct Mol Biol *30*, 339–
1351 347. 10.1038/s41594-023-00923-x.
1352 107. Watts, J.M., Dang, K.K., Gorelick, R.J., Leonard, C.W., Bess, J.W., Jr., Swanstrom,
1353 R., Burch, C.L., and Weeks, K.M. (2009). Architecture and secondary structure of
1354 an entire HIV-1 RNA genome. Nature *460*, 711–716. 10.1038/nature08237.
1355 108. Garcia-Moreno, M., Noerenberg, M., Ni, S., Jarvelin, A.I., Gonzalez-Almela, E.,
1356 Lenz, C.E., Bach-Pages, M., Cox, V., Avolio, R., Davis, T., et al. (2019). System-
1357 wide Profiling of RNA-Binding Proteins Uncovers Key Regulators of Virus
1358 Infection. Mol Cell *74*, 196–211 e111. 10.1016/j.molcel.2019.01.017.
1359 109. Rozman, B., Nachshon, A., Levi Samia, R., Lavi, M., Schwartz, M., and Stern-
1360 Ginossar, N. (2022). Temporal dynamics of HCMV gene expression in lytic and
1361 latent infections. Cell reports *39*, 110653. 10.1016/j.celrep.2022.110653.
1362 110. Burgess, H.M., Grande, R., Riccio, S., Dinesh, I., Winkler, G.S., Depledge, D.P.,
1363 and Mohr, I. (2023). CCR4-NOT differentially controls host versus virus poly(a)-
1364 tail length and regulates HCMV infection. EMBO Rep *24*, e56327.
1365 10.15252/embr.202256327.
1366 111. Derdeyn, C.A., Decker, J.M., Sfakianos, J.N., Wu, X., O'Brien, W.A., Ratner, L.,
1367 Kappes, J.C., Shaw, G.M., and Hunter, E. (2000). Sensitivity of human
1368 immunodeficiency virus type 1 to the fusion inhibitor T-20 is modulated by
1369 coreceptor specificity defined by the V3 loop of gp120. J Virol *74*, 8358–8367.
1370 10.1128/jvi.74.18.8358-8367.2000.
1371 112. Wei, X., Decker, J.M., Liu, H., Zhang, Z., Arani, R.B., Kilby, J.M., Saag, M.S., Wu, X.,
1372 Shaw, G.M., and Kappes, J.C. (2002). Emergence of resistant human
1373 immunodeficiency virus type 1 in patients receiving fusion inhibitor (T-20)
1374 monotherapy. Antimicrob Agents Chemother *46*, 1896–1905.
1375 10.1128/aac.46.6.1896-1905.2002.
1376 113. Platt, E.J., Wehrly, K., Kuhmann, S.E., Chesebro, B., and Kabat, D. (1998). Effects
1377 of CCR5 and CD4 cell surface concentrations on infections by
1378 macrophagetropic isolates of human immunodeficiency virus type 1. J Virol *72*,
1379 2855–2864. 10.1128/JVI.72.4.2855-2864.1998.
1380 114. Antzin-Anduetza, I., Mahiet, C., Granger, L.A., Odendall, C., and Swanson, C.M.
1381 (2017). Increasing the CpG dinucleotide abundance in the HIV-1 genomic RNA
1382 inhibits viral replication. Retrovirology *14*, 49. 10.1186/s12977-017-0374-1.

115. Fouchier, R.A., Meyer, B.E., Simon, J.H., Fischer, U., and Malim, M.H. (1997). HIV-1 infection of non-dividing cells: evidence that the amino-terminal basic region of the viral matrix protein is important for Gag processing but not for post-entry nuclear import. EMBO J *16*, 4531–4539. 10.1093/emboj/16.15.4531.
116. Chen, R.A., Ryzhakov, G., Cooray, S., Randow, F., and Smith, G.L. (2008). Inhibition of IkappaB kinase by vaccinia virus virulence factor B14. PLoS Pathog *4*, e22. 10.1371/journal.ppat.0040022.
117. Lee, F.C.Y., Chakrabarti, A.M., Hänel, H., Monzón-Casanova, E., Hallegger, M., Militti, C., Capraro, F., Sadée, C., Toolan-Kerr, P., Wilkins, O., et al. (2021). An improved iCLIP protocol. bioRxiv, 2021.2008.2027.457890. 10.1101/2021.08.27.457890.
118. Smith, T., Heger, A., and Sudbery, I. (2017). UMI-tools: modeling sequencing errors in Unique Molecular Identifiers to improve quantification accuracy. Genome Res *27*, 491–499. 10.1101/gr.209601.116.
119. Bushnell, B., Rood, J., and Singer, E. (2017). BBMerge - Accurate paired shotgun read merging via overlap. PLoS One *12*, e0185056. 10.1371/journal.pone.0185056.
120. Ewels, P.A., Peltzer, A., Fillinger, S., Patel, H., Alneberg, J., Wilm, A., Garcia, M.U., Di Tommaso, P., and Nahnsen, S. (2020). The nf-core framework for community-curated bioinformatics pipelines. Nat Biotechnol *38*, 276–278. 10.1038/s41587-020-0439-x.
121. West, C., Capitanchik, C., Cheshire, C., Luscombe, N.M., Chakrabarti, A., and Ule, J. (2023). nf-core/clipseq - a robust Nextflow pipeline for comprehensive CLIP data analysis. Wellcome Open Res *8*, 286. 10.12688/wellcomeopenres.19453.1.
122. Di Tommaso, P., Chatzou, M., Floden, E.W., Barja, P.P., Palumbo, E., and Notredame, C. (2017). Nextflow enables reproducible computational workflows. Nat Biotechnol *35*, 316–319. 10.1038/nbt.3820.
123. Frith, M.C., Valen, E., Krogh, A., Hayashizaki, Y., Carninci, P., and Sandelin, A. (2008). A code for transcription initiation in mammalian genomes. Genome Res *18*, 1–12. 10.1101/gr.6831208.
124. Chakrabarti, A.M., Capitanchik, C., Ule, J., and Luscombe, N.M. (2023). clipplotr-a comparative visualization and analysis tool for CLIP data. RNA *29*, 715–723. 10.1261/rna.079326.122.
125. Teufel, F., Almagro Armenteros, J.J., Johansen, A.R., Gislason, M.H., Pihl, S.I., Tsirigos, K.D., Winther, O., Brunak, S., von Heijne, G., and Nielsen, H. (2022). SignalP 6.0 predicts all five types of signal peptides using protein language models. Nat Biotechnol *40*, 1023–1025. 10.1038/s41587-021-01156-3.
126. Stelzer, G., Rosen, N., Plaschkes, I., Zimmerman, S., Twik, M., Fishilevich, S., Stein, T.I., Nudel, R., Lieder, I., Mazor, Y., et al. (2016). The GeneCards Suite: From Gene Data Mining to Disease Genome Sequence Analyses. Current protocols in bioinformatics / editoral board, Andreas D. Baxevanis ... [et al.] *54*, 1 30 31–31 30 33. 10.1002/cpbi.5.
127. Yu, G., Wang, L.G., Han, Y., and He, Q.Y. (2012). clusterProfiler: an R package for comparing biological themes among gene clusters. Omics : a journal of integrative biology *16*, 284–287. 10.1089/omi.2011.0118.

128. Chen, H., and Boutros, P.C. (2011). VennDiagram: a package for the generation of highly-customizable Venn and Euler diagrams in R. BMC bioinformatics *12*, 35. 10.1186/1471-2105-12-35.
129. De Coster, W., D'Hert, S., Schultz, D.T., Cruts, M., and Van Broeckhoven, C. (2018). NanoPack: visualizing and processing long-read sequencing data. Bioinformatics *34*, 2666–2669. 10.1093/bioinformatics/bty149.
130. Li, H. (2018). Minimap2: pairwise alignment for nucleotide sequences. Bioinformatics *34*, 3094–3100. 10.1093/bioinformatics/bty191.
131. Li, H. (2021). New strategies to improve minimap2 alignment accuracy. Bioinformatics *37*, 4572–4574. 10.1093/bioinformatics/btab705.
132. Lawrence, M., Huber, W., Pages, H., Aboyoun, P., Carlson, M., Gentleman, R., Morgan, M.T., and Carey, V.J. (2013). Software for computing and annotating genomic ranges. PLoS computational biology *9*, e1003118. 10.1371/journal.pcbi.1003118.

FIGURE LEGENDS

Figure 1: ZAP isoforms differ in their activity to restrict HIV-CpG and interact with KHNYN and viral RNA.

(A) Schematic representation of the exonucleolytic model for ZMD. Created in BioRender. Bouton, C. (2025) https://BioRender.com/b8wrgls

(B) Schematic representation of the endonucleolytic model for ZMD. Created in BioRender. Bouton, C. (2025) https://BioRender.com/lpjkyv4

(C) Schematic representation of ZAP's main isoforms, ZAP-L and ZAP-S. ZnF: zinc finger. ART-like: ADP-ribosyltransferase-like domain. CaaX: CaaX box that mediates S-farnesylation.

(D) Genomic organization and localization of CpG dinucleotides of HIV-WT and HIV-CpG.

(E) Relative infectious HIV production (left) in HEK293T CRISPR control and ZAP cells, and HIV-CpG production expressed as % infectious HIV-WT production (right). Error bars represent standard deviation. *p <0.05 calculated by one-way ANOVA on log-transformed data, compared to HIV-CpG production in HEK293T CRISPR control cells.

(F) Immunoblotting of uninfected isoform-specific HEK293T CRISPR ZAP cells.

1460 **(G)** Infectious HIV-CpG production, expressed as % infectious HIV-WT production, in
1461 isoform-specific HEK293T CRISPR ZAP cells. Error bars represent standard deviation. *p
1462 <0.05 calculated by one-way ANOVA on log-transformed data, compared to HIV-CpG
1463 production in HEK293T cells.
1464 **(H)** Immunoblotting of ZAP coimmunoprecipitations and corresponding input lysates
1465 obtained from isoform-specific HEK293T CRISPR ZAP cells at steady state level. The
1466 blots are representative of three biological replicates.
1467 **(I)** Normalized ZAP iCLIP signal mapped to HIV-CpG gRNA in isoform-specific HEK293T
1468 CRISPR ZAP cells. The average signal of three independent experiments and the SEM
1469 (shading) are plotted. Localization of CpG dinucleotides on HIV-CpG gRNA are indicated
1470 by vertical bars. Pink bars represent the 36 added CpG dinucleotides in HIV-CpG.
1471
1472 **Figure 2: ZAP-L and ZAP-S bind different CpG-rich motifs and target different cellular**
1473 **transcripts.**
1474 **(A)** Heatmap for the top 10 PEKA motifs from ZAP-S knockout or ZAP-L knockout cell iCLIP
1475 experiments shown for HEK293T, ZAP-S knockout and ZAP-L knockout cells.
1476 **(B)** Normalized DESeq2 counts for TNFRSF10D from poly(A) RNA-seq in HEK293T, ZAP-L
1477 and ZAP-S knockout cells. Error bars represent standard deviation. *adjp <0.05
1478 calculated by DESeq2, compared to HEK293T cells.
1479 **(C)** Normalized DESeq2 counts for JUN from poly(A) RNA-seq in HEK293T, ZAP-L and ZAP-
1480 S knockout cells. Error bars represent standard deviation. *adjp <0.05 calculated by
1481 DESeq2, compared to HEK293T cells.

1482 **(D)** Normalized AP-1 reporter activity in HEK293T, ZAP-L and ZAP-S knockout cells. Error
1483 bars represent standard deviation. *p <0.05 calculated by one-way ANOVA on log-
1484 transformed data, compared to HEK293T cells.
1485 **(E)** % of genes specifically regulated by ZAP-L or ZAP-S predicted to contain a signal
1486 peptide by SignalP - 6.0[125].
1487 **(F)** Normalized crosslink signal for ZAP iCLIP on TNFRSF10D in HEK293T, ZAP-L KO and
1488 ZAP-S KO cells. The average signal of three independent experiments and the SEM
1489 (shading) are plotted. The start and stop codon locations are indicated in pink.
1490
1491 **Figure 3: HIV-1 infection promotes the interaction between TRIM25 and KHNYN.**
1492 **(A)** Immunoblotting of ZAP coimmunoprecipitations and corresponding input lysates
1493 obtained from infected HeLa cells. Samples were treated with RNase I after pulldown and
1494 PABPC1 is a control to indicate that the RNase I treatment reduced RNA-dependent
1495 interactions. The blots are representative of three biological replicates.
1496 **(B)** Immunoblotting of TRIM25 coimmunoprecipitations and corresponding input lysates
1497 obtained from infected HeLa cells. Samples were treated with RNase I after pulldown.
1498 Note that the experiment shown here was performed alongside the experiment shown in
1499 Figure 5E, thus the input blots for TRIM25, PABPC1, GAPDH, and gp160/gp120 and
1500 pulldown blots for TRIM25 and PABPC1 are identical between the two figures. The blots
1501 are representative of three biological replicates.
1502 **(C)** Immunoblotting of ZAP coimmunoprecipitations and corresponding input lysates
1503 obtained from infected Control and TRIM25 CRISPR HeLa cells. Samples were treated
1504 with RNase I after pulldown. Note that the experiment shown here was performed
1505 alongside the experiment shown in Figure S9I, thus the input blots for PABPC1, TRIM25,

ZAP and GAPDH and pulldown blots for PABPC1, TRIM25 and ZAP are identical between the two panels. The blots are representative of three biological replicates.

(D-E) Hallmark gene set enrichment plot of differentially expressed genes in HIV-WT **(D)** or HIV-CpG **(E)** infected HeLa CRISPR control cells. Black dots are non-significant, blue and pink dots are significant. Pink dots show functional groups highlighted in the text.

Figure 4: HIV-1 infection increases the number of cellular genes that are co-upregulated by ZAP, TRIM25, and KHNYN.

(A) Heat map indicating differentially expressed genes that are co-upregulated in ZAP, TRIM25 and KHNYN CRISPR cells compared to CRISPR Control cells in mock, HIV-WT or HIV-CpG infected cells.

(B) Number of genes co-upregulated by ZAP, TRIM25 and KHNYN in mock, HIV-WT and HIV-CpG infected cells.

(C) GO analysis for ZAP, TRIM25 and KHNYN co-regulated genes with FDR <0.1 in HIV-WT infected cells.

(D) Normalized DESeq2 counts for ZMAT3 from poly(A) RNA-seq in mock or HIV-WT infected Control, ZAP, TRIM25 or KHNYN CRISPR cells. Error bars represent standard deviation. *adjp <0.05 calculated by DESeq2, compared to Control CRISPR cells.

(E) Normalized ZAP iCLIP signal mapped to ZMAT3 in HIV-WT infected Control CRISPR cells. The average signal of three independent experiments and the SEM (shading) are plotted. Exon tracks represent the isoforms expressed >1% of total normalized DESeq2 counts. The start and stop codon locations are indicated in pink.

1528 **(F)** Normalized DESeq2 counts for HSPB8 from poly(A) RNA-seq in mock or HIV-WT
1529 infected Control, ZAP, TRIM25 or KHNYN CRISPR cells. Error bars represent standard
1530 deviation. *adjp <0.05 calculated by DESeq2, compared to Control CRISPR cells.
1531 **(G)** Normalized ZAP iCLIP signal mapped to HSPB8 in HIV-WT infected Control CRISPR
1532 cells. The average signal of three independent experiments and the SEM (shading) are
1533 plotted. Exon tracks represent the isoforms expressed >1% of total normalized DESeq2
1534 counts. The start and stop codon locations are indicated in pink.
1535
1536 **Figure 5: Degradation of HIV-CpG 3' cleavage fragment by XRN1.**
1537 **(A)** KHNYN iCLIP signal mapped to HIV-CpG gRNA in HeLa CRISPR KHNYN + GFP and
1538 HeLa CRISPR KHNYN + CRISPR-resistant KHNYN-GFP. The average signal of three
1539 independent experiments and the SEM (shading) are plotted.
1540 **(B)** Genomic organization of HIV-WT and HIV-CpG and localization of CpG dinucleotides.
1541 The qRT-PCR probe used to quantify the 3' cleavage fragment (probe 2 (p2)), and the HIV
1542 specific primer used for the 5' RACE (5'R) are shown.
1543 **(C)** Level of HIV-CpG 3' cleavage fragment measured by qRT-PCR in cells transfected with
1544 siRNA targeting XRN1. Results are expressed as % 3' cleavage fragment in HIV-WT
1545 infected cells. The dotted line represents the level of 3' cleavage fragment in cells treated
1546 with a non-targeting siRNA control. Error bars represent standard deviation. *p <0.05
1547 calculated by one-way ANOVA on log-transformed data, compared to the level of 3'
1548 cleavage fragment in cells treated with a non-targeting siRNA control.
1549 **(D)** Immunoblotting of ZAP coimmunoprecipitations and corresponding input lysates
1550 obtained from infected HeLa cells. Samples were treated with RNase I after pulldown.
1551 The blots are representative of three biological replicates.

1552 **(E)** Immunoblotting of TRIM25 coimmunoprecipitations and corresponding input lysates
1553 obtained from infected HeLa cells. Samples were treated with RNase I after pulldown.
1554 Note that the experiment shown here was performed alongside the experiment shown in
1555 Figure 3B, thus the input blots for gp160/gp120, PABPC1, TRIM25, and GAPDH and the
1556 pulldown blots for PABPC1 and TRIM25 are identical between the two figures. The blots
1557 are representative of three biological replicates.
1558 **(F)** Agarose gel electrophoresis of 5' RACE reactions. Sizes in kilobases are indicated on
1559 the left.
1560 **(G)** 5' RACE DNA was sequenced by long-read sequencing and the 5' end of each
1561 molecule was identified and mapped onto HIV gRNA. The number of 5' end at every
1562 position was determined and compared between experimental conditions. iCLIP signals
1563 for ZAP (from Figure S6B) and KHNYN (from panel A) are shown for reference.
1564
1565 **Figure 6: HIV-CpG 5' cleavage fragment abundance is regulated by TUT4/TUT7 and**
1566 **DIS3L2.**
1567 **(A)** Agarose gel electrophoresis of 3' RACE reactions. Sizes in kilobases are indicated on
1568 the left.
1569 **(B)** Non-templated nucleotides are found in the 3' end of HIV-CpG 5' cleavage fragments
1570 amplified by 3' RACE and determined by Sanger sequencing. The 3' end positions shown
1571 here all fall within the CpG-enriched region of HIV-CpG.
1572 **(C)** Level of HIV-CpG 5' cleavage fragment measured by qRT-PCR in cells transfected with
1573 siRNA targeting TUTs and DIS3L2. Results are expressed as % 5' cleavage fragment in HIV-
1574 WT infected cells. The dotted line represents the level of 5' cleavage fragment in cells
1575 treated with a non-targeting siRNA control. Error bars represent standard deviation. *p

1576 <0.05 calculated by one-way ANOVA on log-transformed data, compared to the level of
1577 5' cleavage fragment in cells treated with a non-targeting siRNA control.
1578 **(D)** 3' RACE DNA was sequenced by long-read sequencing and the 3' end of each
1579 molecule was identified and mapped onto HIV gRNA. The number of 3' end at every
1580 position was determined and compared between experimental conditions. iCLIP signals
1581 for ZAP (from Figure S6B) and KHNYN (from Figure 5A) are shown for reference.
1582 **(E)** The sequence and length of non-templated nucleotides was extracted for every
1583 sequenced 3' end in HIV-CpG infected cells transfected with siRNA control or siRNA
1584 targeting ZAP or DIS3L2.
1585
1586 **Figure 7: Model of the ZAP-mediated RNA decay**
1587 A ZAP-L-TRIM25-KHNYN complex assembles on clustered CpG dinucleotides. This leads
1588 to RNA cleavage by KHNYN. The 3' cleavage fragment is then degraded by the 5'-3'
1589 exonuclease XRN1, while the 5' cleavage fragment is uridylated by TUT4/7 and then
1590 degraded by the 3'-5' exonuclease DIS3L2. ZAP interacts with each component of the
1591 complex. Created in BioRender. Bouton, C. (2025) https://BioRender.com/f8zm1lm
1592
1593 **SUPPLEMENTAL FIGURE LEGENDS**
1594 **Figure S1: ZAP isoforms differ in their activity and their interaction with viral RNA,**
1595 **related to Figure 1.**
1596 **(A)** Relative infectious virus production in isoform-specific HEK293T CRISPR ZAP cells.
1597 The dotted line represents HIV-CpG production in HEK293T cells. Error bars represent
1598 standard deviation.

1599 **(B)** Immunoblotting of cell lysates and virions from HIV-WT- or HIV-CpG-infected isoform-
1600 specific HEK293T CRISPR ZAP cells.
1601 **(C)** Quantification of KHNYN and TRIM25 abundance in the ZAP PULL-DOWN
1602 immunoblot from panel 1H. The signal was normalized ZAP abundance in the ZAP PULL-
1603 DOWN samples. Error bars represent standard deviation. *p <0.05 calculated by one-way
1604 ANOVA on log-transformed data, compared to HEK293T cells.
1605 **(D-F)** Normalized ZAP iCLIP signal mapped to HIV gRNA in HEK293T cells **(D)**, HEK293T
1606 ZAP-L KO **(E)** and HEK293T ZAP-S KO **(F)**. The average of three independent experiments
1607 and the SEM (shading) are plotted.
1608 **(G)** ZAP binding peaks on HIV-CpG RNA in 293T cells. Peaks were called by Clippy and
1609 their width are indicated.
1610 **(H)** Quantification of normalized crosslink signal in Peak1 and Peak 3 for Figure S1D. Error
1611 bars represent standard deviation. *p <0.05 calculated by unpaired t test on log-
1612 transformed data, compared to HIV-WT.
1613 **(I)** Quantification of normalized crosslink signal in Peak1, Peak 2 and Peak 3 for Figure 1I.
1614 Error bars represent standard deviation. *p <0.05 calculated by unpaired t test on log-
1615 transformed data, compared to 293T cells.
1616
1617 **Figure S2: ZAP-L and ZAP-S bind different motifs, target different cellular transcripts**
1618 **and have differential subcellular localization that is not affected by HIV-CpG**
1619 **infection, related to Figure 2.**
1620 **(A)** UpA + CpG motifs ranked in the top 15 from the ZAP iCLIP experiments in ZAP-S
1621 knockout cells and their corresponding rank in HEK293T and ZAP-L KO cells.

1622 **(B)** GO analysis for ZAP-L regulated genes with FDR <0.1 in HIV-WT infected cells. The FDR
1623 for the same terms for ZAP-S regulated genes are shown.
1624 **(C)** GO analysis for ZAP-S regulated genes with FDR <0.1 in HIV-WT infected cells. The
1625 FDR for the same terms for ZAP-L regulated genes are shown.
1626 **(D-F)** Normalized DESeq2 counts for JUNB **(D)**, JUND **(C)** and FOS **(F)** from poly(A) RNA-
1627 seq in HEK293T, ZAP-L and ZAP-S knockout cells. Error bars represent standard deviation.
1628 *adjp <0.05 calculated by DESeq2, compared to HEK293T cells.
1629 **(G)** ZAP, ER (RTN4) and HIV-1 genomic RNA localization in mock or HIV-CpG infected
1630 HEK293T, ZAP-L KO or ZAP-S KO cells detected using indirect immunofluorescence for
1631 ZAP and RTN4 (an ER resident protein) plus RNA FISH for HIV-1 genomic RNA.
1632
1633 **Figure S3: ZAP binding peaks in TNFRSF10D have interspersed UpA and CpG**
1634 **dinucleotides, related to Figure 2.** ZAP binding peaks in TNFRSF10D identified in ZAP-S
1635 knockout cells using clippy. UpA dinucleotides are highlighted in yellow, CpG
1636 dinucleotides are highlighted in blue and UACG motifs are highlighted in green.
1637
1638 **Figure S4: HIV-1 infection increases the number of ZAP, TRIM25 or KHNYN-regulated**
1639 **genes, related to Figure 3 and 4.**
1640 **(A)** Quantification of KHNYN abundance in the TRIM25 PULL-DOWN immunoblot from
1641 panel 3B. The signal was normalized to TRIM25 abundance in the TRIM25 PULL-DOWN
1642 samples. Error bars represent standard deviation.
1643 **(B)** Heat map indicating differentially expressed genes that are upregulated in ZAP,
1644 TRIM25 or KHNYN CRISPR cells compared to CRISPR control cells in mock, HIV-WT or
1645 HIV-CpG infected cells.

1646 **(C)** Number of upregulated genes in ZAP, KHNYN or TRIM25 knockout cells compared to
1647 CRISPR control cells in mock, HIV-WT or HIV-CpG infected cells.
1648 **(D)** Euler diagrams showing differentially expressed genes that are upregulated in ZAP,
1649 TRIM25 or KHNYN CRISPR cells compared to CRISPR control cells in mock, HIV-WT or
1650 HIV-CpG infected cells.
1651
1652 **Figure S5: ZAP, TRIM25 and KHNYN co-regulate a subset of genes downregulated by**
1653 **HIV-1 infection and ZAP-L mRNA, related to Figure 4.**
1654 **(A)** Euler diagram showing differentially expressed genes that are upregulated in ZAP,
1655 TRIM25 or KHNYN CRISPR cells compared to CRISPR control cells in mock, HIV-WT or
1656 HIV-CpG infected cells and downregulated by HIV-WT infection.
1657 **(B)** Normalized DESeq2 counts for DIO2 from poly(A) RNA-seq in mock or HIV-WT
1658 infected Control, ZAP, TRIM25 or KHNYN knockout cells. Error bars represent standard
1659 deviation. *adjp <0.05 calculated by DESeq2, comparing HIV-WT infected Control
1660 CRISPR cells to mock infected Control CRISPR cells. *adjp <0.05 calculated by DESeq2,
1661 comparing HIV-WT infected ZAP, TRIM25 or KHNYN CRISPR cells to HIV-WT infected
1662 Control CRISPR cells.
1663 **(C)** Normalized ZAP iCLIP signal mapped to DIO2 in HIV-WT infected Control CRISPR
1664 cells. The average signal of three independent experiments and the SEM (shading) are
1665 plotted. Exon tracks represent the isoforms expressed >1% of total normalized DESeq2
1666 counts. The start and stop codon locations are indicated in pink.
1667 **(D-E)** Normalized ZAP iCLIP signal mapped to ZAP-L **(D)** or ZAP-S **(E)** mRNA in HIV-WT
1668 infected Control CRISPR cells. The average signal of three independent experiments and
1669 the SEM (shading) are plotted. The normalized ZAP crosslink signal was distributed to

1670 ZAP-L or ZAP-S based on the isoform's normalized DESeq2 count. Exons are indicated in
1671 grey and start and stop codon locations are in pink.
1672 **(F)** Immunoblotting of mock, HIV-WT and HIV-CpG infected Control, ZAP, TRIM25 or
1673 KHNYN CRISPR cells.
1674 **(G)** Relative infectious HIV-1 production (left) in Control, ZAP, TRIM25 and KHNYN
1675 CRISPR cells, and HIV-CpG production expressed as % infectious HIV-WT production
1676 (right). Error bars represent standard deviation. *p <0.05 calculated by one-way ANOVA
1677 on log-transformed data, compared to HIV-CpG production in Control CRISPR control
1678 cells.
1679 **(H)** Normalized DESeq2 counts for ZAP-L mRNA from poly(A) RNA-seq in mock or HIV-WT
1680 infected Control, ZAP, TRIM25 or KHNYN knockout cells. Error bars represent standard
1681 deviation. *adjp <0.05 calculated by DESeq2, compared to Control CRISPR cells.
1682
1683 **Figure S6: TRIM25 modulates ZAP binding to HIV-CpG RNA but does not alter its**
1684 **target specificity, related to Figure 4.**
1685 **(A)** Relative levels of ZAP-associated HIV-1 gRNA measured by qRT-PCR in HeLa Control
1686 CRISPR (left) and TRIM25 CRISPR (right) cells transfected with proviral DNA. Error bars
1687 represent standard deviation. *p <0.05 calculated by unpaired two-tailed t test,
1688 compared to ZAP-associated HIV-WT gRNA.
1689 **(B)** ZAP iCLIP signal mapped to HIV-CpG gRNA in HeLa CRISPR TRIM25 and control. The
1690 average signal of three independent experiments and the SEM (shading) are plotted.
1691 **(C)** Quantification of normalized crosslink signal in Peak1, Peak 2 and Peak 3 for Figure
1692 S6B. Error bars represent standard deviation. *p <0.05 calculated by unpaired t test on
1693 log-transformed data, compared to HIV-WT.

1694 **(D)** MA plot showing genes with differential iCLIP read abundance in HIV-WT infected
1695 TRIM25 CRISPR cells compared to Control CRISPR cells.
1696 **(E)** Normalized ZAP iCLIP signal mapped to ZAP in HIV-WT infected Control CRISPR cells.
1697 The average signal of three independent experiments and the SEM (shading) are plotted.
1698 Exon for ZAP-L and ZAP-S mRNAs are represented in grey and the start and stop codon
1699 locations are in pink.
1700 **(F)** Heatmap showing the top 15 PEKA motifs from ZAP iCLIP experiments in CRISPR
1701 control cells and their relative rank in TRIM25 CRISPR cells.
1702 **(G)** Euler diagram of genes encoding transcripts with ZAP peaks in HIV-WT infected
1703 CRISPR control and TRIM25 knockout cells.
1704
1705 **Figure S7: Depletion of CNOT1, PARN, EXOSC3, EXOSC5, EXOSC7, DDX17, DHX30 or**
1706 **DCP2 does not affect HIV-CpG infectious virus production, related to Figure 5.**
1707 **(A)** Top 25 PEKA motifs for KHNYN iCLIP. CpG and UpA motifs are highlighted in red.
1708 **(B)** Infectious HIV-CpG production, expressed as % infectious HIV-WT production in HeLa
1709 cells transfected with siRNA targeting ZAP, TRIM25 or KHNYN. The dotted line represents
1710 HIV-CpG production in cells transfected with a non-targeting control siRNA. Error bars
1711 represent standard deviation. *p <0.05 calculated by one-way ANOVA on log-
1712 transformed data, compared to HIV-CpG production in cells treated with a non-targeting
1713 siRNA control.
1714 **(C-D)** Infectious HIV-CpG production, expressed as % infectious HIV-WT production in
1715 HeLa cells transfected with siRNA targeting potential ZAP cofactors. The dotted line
1716 represents HIV-CpG production in cells transfected with a non-targeting control siRNA.
1717 Error bars represent standard deviation. *p <0.05 calculated by one-way ANOVA on log-

1718 transformed data, compared to HIV-CpG production in cells treated with a non-targeting
1719 siRNA control.
1720 **(E)** Immunoblotting of HeLa cells transfected with siRNA targeting the genes in (B) and
1721 (C), then infected with HIV-WT.
1722 **(F-G)** Level of HIV-CpG 3' cleavage fragment measured by qRT-PCR in cells transfected
1723 with siRNA targeting potential ZAP cofactors. Results are expressed as % 3' cleavage
1724 fragment in HIV-WT infected cells. The dotted line represents the level of 3' cleavage
1725 fragment in cells treated with a non-targeting siRNA control. Error bars represent
1726 standard deviation. *p <0.05 calculated by one-way ANOVA on log-transformed data,
1727 compared to the level of 3' cleavage fragment in cells treated with a non-targeting siRNA
1728 control.
1729 **(H)** Quantification of XRN1 abundance in the TRIM25 PULL-DOWN immunoblot from
1730 panel 5E. The signal was normalized TRIM25 abundance in the TRIM25 PULL-DOWN
1731 samples. Error bars represent standard deviation.
1732 **(I)** Immunoblotting of ZAP coimmunoprecipitations and corresponding input lysates
1733 obtained from infected Control and TRIM25 CRISPR HeLa cells. Samples were treated
1734 with RNase I after pulldown. Note that the experiment shown here was performed
1735 alongside the experiment shown in Figure S10G, thus the input blots for PABPC1, TRIM25,
1736 ZAP and GAPDH are identical between the two panels. The blots are representative of
1737 three biological replicates.
1738
1739 **Figures S8: Clustered endonuclease cleavage sites correlate with high levels of ZAP**
1740 **binding, related to Figure 5**

1741 **(A)** Normalized ZAP crosslink signal (top panel), KHNYN crosslink signal (middle panel)
1742 and HIV-CpG / HIV-WT fold change in 5' end coverage in XRN1 knockout cells (bottom
1743 panel).
1744 **(B)** HIV-CpG sequence nt 6000-6700. CpG is highlighted in blue, UpA is highlighted in
1745 yellow and UACG is highlighted in green. Cleavage sites are indicated by a red slash.
1746
1747 **Figure S9: Depletion of CNOT1, PARN, EXOSC3, EXOSC5, EXOSC7, XRN1, DDX17, or**
1748 **DHX30 does not affect the abundance of the 5' HIV-CpG RNA cleavage fragment,**
1749 **related to Figure 6.**
1750 **(A)** Genomic organization of HIV-WT and HIV-CpG and localization of CpG dinucleotides.
1751 The qRT-PCR primer/probe set used to quantify the 5' cleavage fragment (probe 1 (p1))
1752 and the HIV-specific primer used for the 3' RACE (3'R) are shown.
1753 **(B)** Level of HIV-CpG 5' cleavage fragment measured by qRT-PCR in cells transfected with
1754 siRNA targeting potential ZAP cofactors. Results are expressed as % 5' cleavage fragment
1755 in HIV-WT infected cells. The dotted line represents the level of 5' cleavage fragment in
1756 cells treated with a non-targeting siRNA control. Error bars represent standard deviation.
1757 *p <0.05 calculated by one-way ANOVA on log-transformed data, compared to the level
1758 of 3' cleavage fragment in cells treated with a non-targeting siRNA control.
1759 **(C)** Immunoblotting of HeLa cells transfected with siRNA targeting TUT4 and TUT7 then
1760 infected with HIV-WT.
1761 **(D)** Infectious HIV-CpG production, expressed as % infectious HIV-WT production in
1762 HeLa cells transfected with siRNA targeting TUTs. The dotted line represents HIV-CpG
1763 production in cells transfected with a non-targeting control siRNA. Error bars represent

1764 standard deviation. *p <0.05 calculated by one-way ANOVA on log-transformed data,
1765 compared to HIV-CpG production in cells treated with a non-targeting siRNA control.
1766 **(E)** Level of HIV-CpG 3' cleavage fragment measured by qRT-PCR in cells transfected with
1767 siRNA targeting TUTs. Results are expressed as % 3' cleavage fragment in HIV-WT infected
1768 cells. The dotted line represents the level of 3' cleavage fragment in cells treated with a
1769 non-targeting siRNA control. Error bars represent standard deviation. *p <0.05 calculated
1770 by one-way ANOVA on log-transformed data, compared to the level of 3' cleavage
1771 fragment in cells treated with a non-targeting siRNA control.
1772 **(F)** Immunoblotting of ZAP coimmunoprecipitations and corresponding input lysates
1773 obtained from infected HeLa cells. Samples were treated with RNase I after pulldown.
1774 The blots are representative of three biological replicates.
1775 **(G)** Immunoblotting of TRIM25 coimmunoprecipitations and corresponding input lysates
1776 obtained from infected HeLa cells. Samples were treated with RNase I after pulldown.
1777 The blots are representative of three biological replicates.
1778 **(H)** Quantification of TUT7 abundance in the TRIM25 PULL-DOWN immunoblot from
1779 panel S6G. The signal was normalized to TRIM25 abundance in the TRIM25 PULL-DOWN
1780 samples. Error bars represent standard deviation. *p <0.05 calculated by one-way
1781 ANOVA on log-transformed data.
1782 **(I)** Immunoblotting of ZAP coimmunoprecipitations and corresponding input lysates
1783 obtained from infected Control and TRIM25 CRISPR HeLa cells. Samples were treated
1784 with RNase I after pulldown. Note that the experiment shown here was performed
1785 alongside the experiment shown in Figure 3C, thus the input blots for PABPC1, TRIM25,
1786 ZAP and GAPDH are identical between the two panels. The blots are representative of
1787 three biological replicates.

1788

1789

1790 **Figure S10: Depletion of DIS3L2 does not affect HIV-CpG infectious virus production**

1791 **or abundance of the 3' cleavage fragment, related to Figure 6.**

1792 **(A)** Immunoblotting of HeLa cells transfected with siRNA targeting DIS3L2 then infected

1793 with HIV-WT.

1794 **(B)** Level of HIV-CpG 3' cleavage fragment measured by qRT-PCR in cells transfected with

1795 siRNA targeting DIS3L2. Results are expressed as % 3' cleavage fragment in HIV-WT

1796 infected cells. The dotted line represents the level of 3' cleavage fragment in cells treated

1797 with a non-targeting siRNA control. Error bars represent standard deviation. *p <0.05

1798 calculated by one-way ANOVA on log-transformed data, compared to the level of 5'

1799 cleavage fragment in cells treated with a non-targeting siRNA control. This experiment

1800 was performed alongside the experiment shown in figure S9E and therefore shared the

1801 same control and ZAP values.

1802 **(C)** Infectious HIV-CpG production, expressed as % infectious HIV-WT production in

1803 HeLa cells transfected with siRNA targeting DIS3L2. The dotted line represents HIV-CpG

1804 production in cells transfected with a non-targeting control siRNA. Error bars represent

1805 standard deviation. *p <0.05 calculated by one-way ANOVA on log-transformed data,

1806 compared to HIV-CpG production in cells treated with a non-targeting siRNA control. This

1807 experiment was performed alongside the experiment shown in figure 9E and therefore

1808 shared the same control and ZAP values.

1809 **(D)** Immunoblotting of ZAP coimmunoprecipitations and corresponding input lysates

1810 obtained from infected HeLa cells. Samples were treated with RNase I after pulldown.

1811 The blots are representative of three biological replicates.

1812 **(E)** Immunoblotting of TRIM25 coimmunoprecipitations and corresponding input lysates
1813 obtained from infected HeLa cells. Samples were treated with RNase I after pulldown.
1814 The blots are representative of three biological replicates.
1815 **(F)** Quantification of DIS3L2 abundance in the TRIM25 PULL-DOWN immunoblot from
1816 panel S10E. The signal was normalized to TRIM25 abundance in the TRIM25 PULL-DOWN
1817 samples. Error bars represent standard deviation.
1818 **(G)** Immunoblotting of ZAP coimmunoprecipitations and corresponding input lysates
1819 obtained from infected Control and TRIM25 CRISPR HeLa cells. Samples were treated
1820 with RNase I after pulldown. Note that the experiment shown here was performed
1821 alongside the experiment shown in Figure 7I, thus the input blots for PABPC1, TRIM25,
1822 ZAP and GAPDH are identical between the two panels. The blots are representative of
1823 three biological replicates.
1824
1825 **SUPPLEMENTARY DATASETS**
1826
1827 **Table S1: poly(A)RNA-seq in mock, HIV-WT and HIV-CpG infected HEK293T, ZAP-L**
1828 **and ZAP-S knockout cells, related to Figure 1 and 2.**
1829
1830 **Table S2: ZAP binding peaks in HIV-WT and HIV-CpG infected HEK293T, ZAP-L and**
1831 **ZAP-S knockout cells, related to Figure 1 and 2.**
1832
1833 **Table S3: poly(A)RNA-seq in mock, HIV-WT and HIV-CpG infected Control, ZAP,**
1834 **TRIM25 and KHNYN CRISPR cells, related to Figure 3 and 4.**
1835

1836 **Table S4: ZAP binding peaks in HIV-WT and HIV-CpG infected Control and TRIM25**

1837 **CRISPR cells, related to Figure S6.**

1838

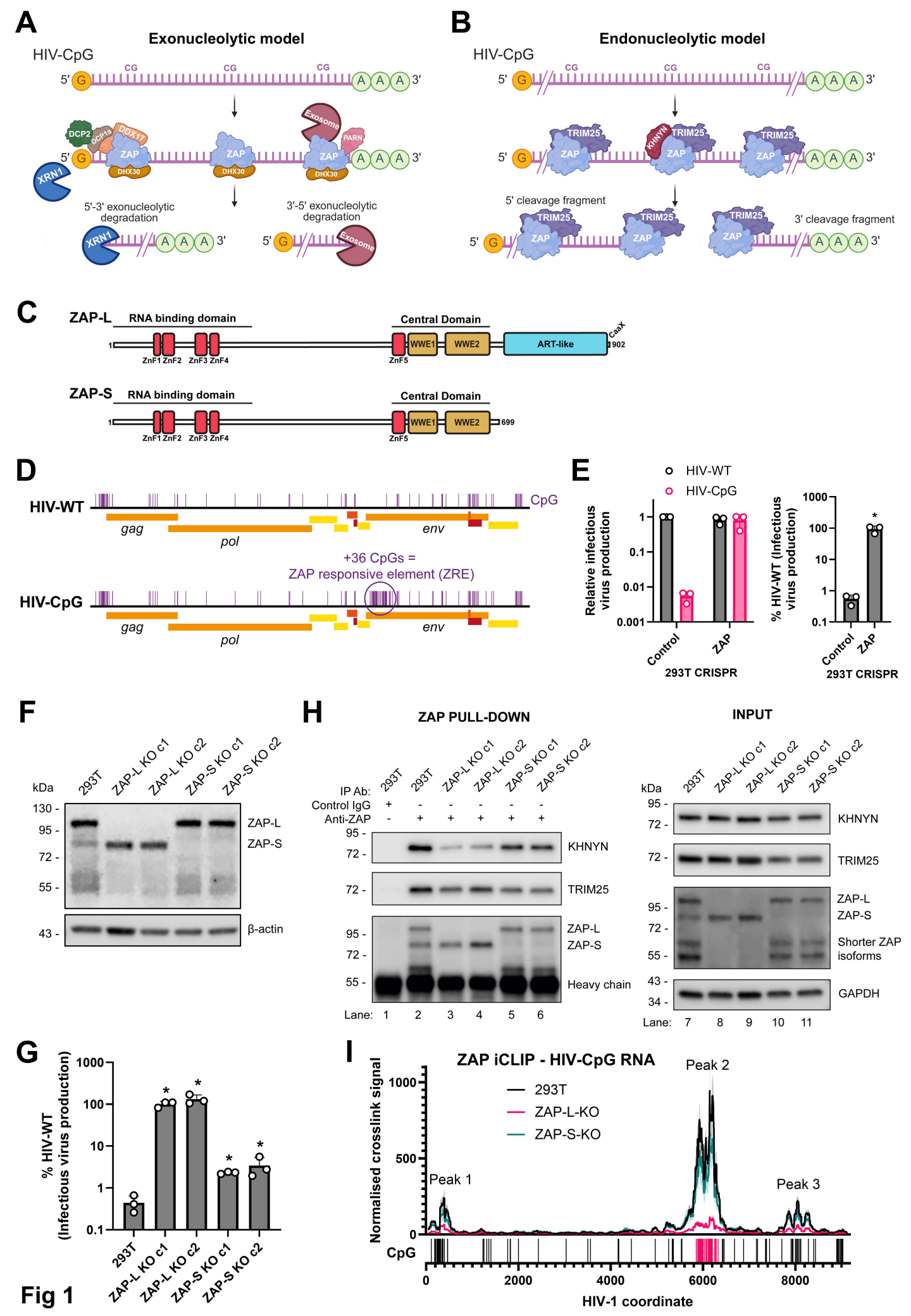
A
Exonucleolytic model
HIV-CpG
5'
G
CG
CG
CG
A A A
3'
DCP2
DCP1a
DDX17
ZAP
DHX30
XRN1
Exosome
PARN
5'-3' exonucleolytic degradation
3'-5' exonucleolytic degradation
B
Endonucleolytic model
TRIM25
KHNYN
5' cleavage fragment
3' cleavage fragment
C
ZAP-L
RNA binding domain
Central Domain
ZnF1 ZnF2
ZnF3 ZnF4
ZnF5
WWE1
WWE2
ART-like
CaaX
1
902
ZAP-S
699
D
HIV-WT
CpG
gag
pol
env
+36 CpGs =
ZAP responsive element (ZRE)
HIV-CpG
E
HIV-WT
HIV-CpG
Relative infectious virus production
% HIV-WT (Infectious virus production)
Control
ZAP
293T CRISPR
F
kDa
293T
ZAP-L KO c1
ZAP-L KO c2
ZAP-S KO c1
ZAP-S KO c2
130 -
95 -
72 -
55 -
43 -
ZAP-L
ZAP-S
β-actin
H
ZAP PULL-DOWN
INPUT
IP Ab:
Control IgG
Anti-ZAP
KHNYN
TRIM25
Heavy chain
Lane: 1 2 3 4 5 6
GAPDH
Shorter ZAP isoforms
Lane: 7 8 9 10 11
G
% HIV-WT (Infectious virus production)
I
ZAP iCLIP - HIV-CpG RNA
293T
ZAP-L-KO
ZAP-S-KO
Peak 1
Peak 2
Peak 3
Normalised crosslink signal
CpG
HIV-1 coordinate

Fig 1

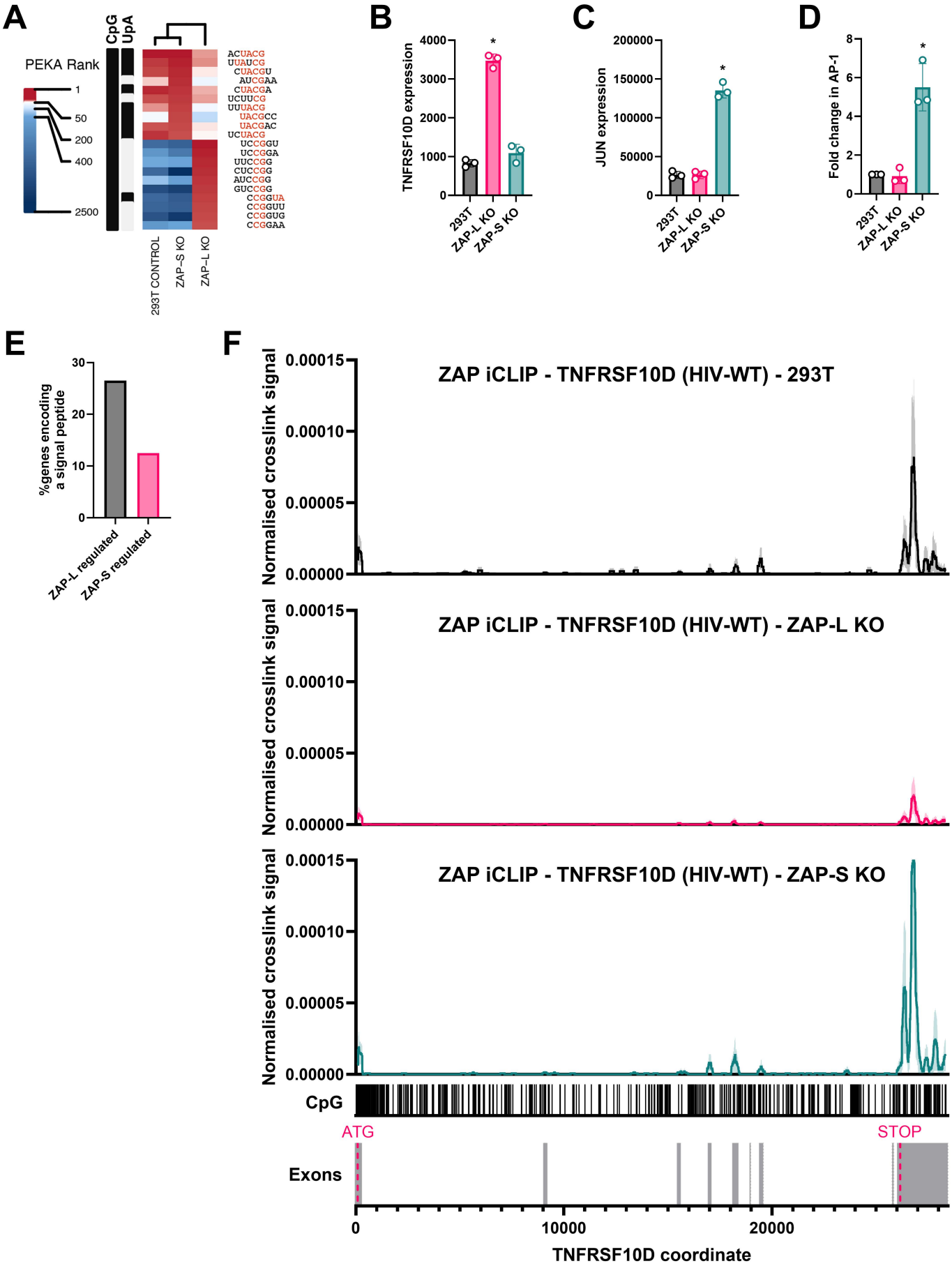
A
CpG
UpA
PEKA Rank
1
50
200
400
2500
ACUACG
UUAUCG
CUACGU
AUCGAA
CUACGA
UCUUCG
UUUACG
UACGCC
UACGAC
UCUACG
UCCGGU
UCCGGA
UUCCGG
CUCCGG
AUCCGG
GUCCGG
CCGGUA
CCGGUU
CCGGUG
CCGGAA
293T CONTROL
ZAP-S KO
ZAP-L KO
B
TNFRSF10D expression
4000
3000
2000
1000
0
*
293T
ZAP-L KO
ZAP-S KO
C
JUN expression
200000
150000
100000
50000
0
*
293T
ZAP-L KO
ZAP-S KO
D
Fold change in AP-1
8
6
4
2
0
*
293T
ZAP-L KO
ZAP-S KO
E
%genes encoding a signal peptide
30
20
10
0
ZAP-L regulated
ZAP-S regulated
F
ZAP iCLIP - TNFRSF10D (HIV-WT) - 293T
ZAP iCLIP - TNFRSF10D (HIV-WT) - ZAP-L KO
ZAP iCLIP - TNFRSF10D (HIV-WT) - ZAP-S KO
Normalised crosslink signal
0.00015
0.00010
0.00005
0.00000
CpG
ATG
STOP
Exons
0
10000
20000
TNFRSF10D coordinate

Fig 2

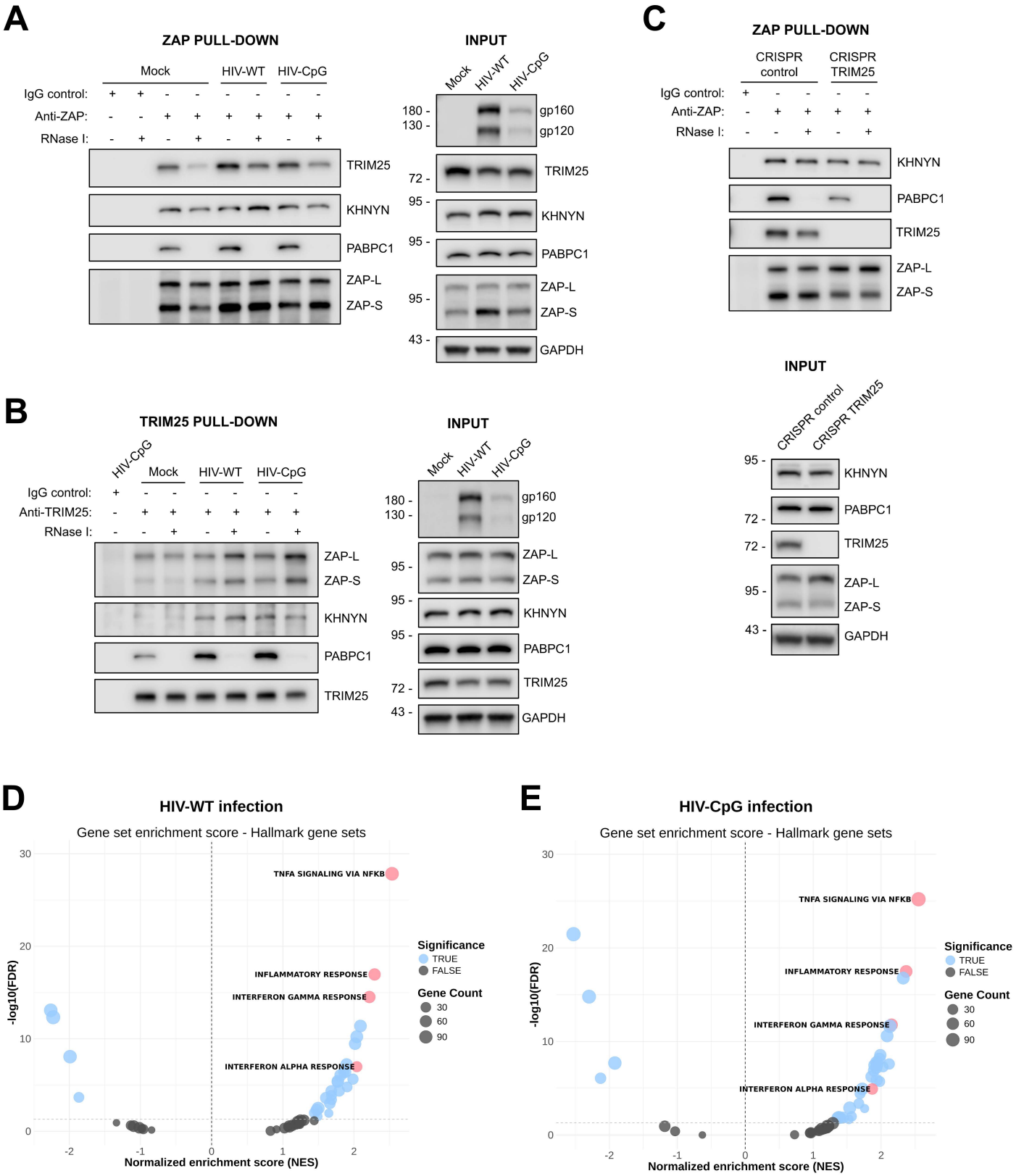
A
ZAP PULL-DOWN
Mock
HIV-WT
HIV-CpG
IgG control:
Anti-ZAP:
RNase I:
TRIM25
KHNYN
PABPC1
ZAP-L
ZAP-S
INPUT
Mock
HIV-WT
HIV-CpG
180 -
130 -
gp160
gp120
72 -
95 -
43 -
GAPDH
B
TRIM25 PULL-DOWN
HIV-CpG
Mock
HIV-WT
HIV-CpG
IgG control:
Anti-TRIM25:
RNase I:
ZAP-L
ZAP-S
KHNYN
PABPC1
TRIM25
INPUT
Mock
HIV-WT
HIV-CpG
C
ZAP PULL-DOWN
CRISPR control
CRISPR TRIM25
IgG control:
Anti-ZAP:
RNase I:
KHNYN
PABPC1
TRIM25
ZAP-L
ZAP-S
INPUT
CRISPR control
CRISPR TRIM25
D
HIV-WT infection
Gene set enrichment score - Hallmark gene sets
TNFA SIGNALING VIA NFKB
INFLAMMATORY RESPONSE
INTERFERON GAMMA RESPONSE
INTERFERON ALPHA RESPONSE
-log10(FDR)
Normalized enrichment score (NES)
Significance
TRUE
FALSE
Gene Count
30
60
90
E
HIV-CpG infection
Gene set enrichment score - Hallmark gene sets
TNFA SIGNALING VIA NFKB
INFLAMMATORY RESPONSE
INTERFERON GAMMA RESPONSE
INTERFERON ALPHA RESPONSE
-log10(FDR)
Normalized enrichment score (NES)
Significance
TRUE
FALSE
Gene Count
30
60
90

Fig 3

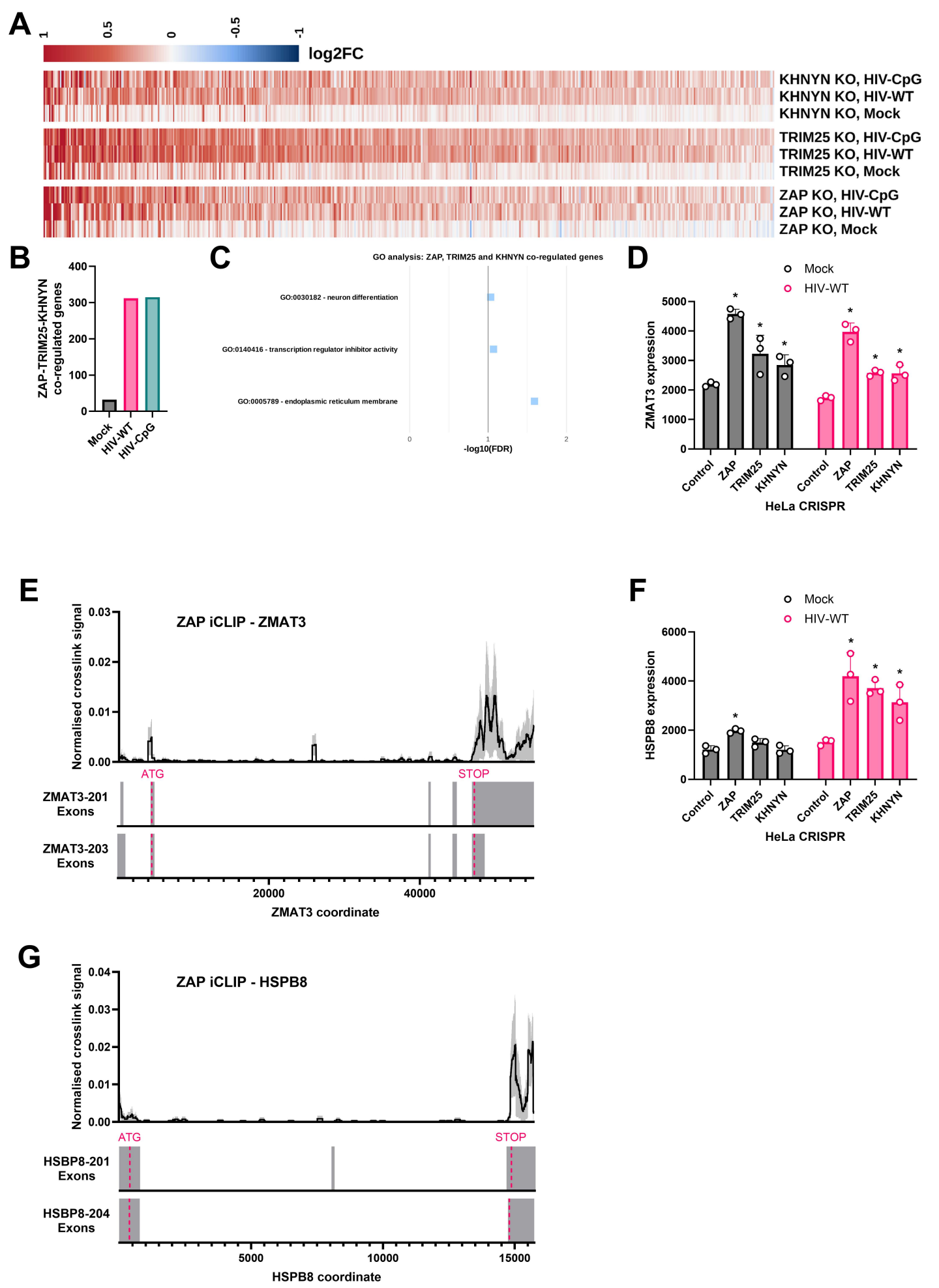
A
1
0.5
0
-0.5
-1
log2FC
KHNYN KO, HIV-CpG
KHNYN KO, HIV-WT
KHNYN KO, Mock
TRIM25 KO, HIV-CpG
TRIM25 KO, HIV-WT
TRIM25 KO, Mock
ZAP KO, HIV-CpG
ZAP KO, HIV-WT
ZAP KO, Mock
B
ZAP-TRIM25-KHNYN co-regulated genes
400
300
200
100
0
Mock
HIV-WT
HIV-CpG
C
GO analysis: ZAP, TRIM25 and KHNYN co-regulated genes
GO:0030182 - neuron differentiation
GO:0140416 - transcription regulator inhibitor activity
GO:0005789 - endoplasmic reticulum membrane
0
1
2
-log10(FDR)
D
Mock
HIV-WT
ZMAT3 expression
5000
4000
3000
2000
1000
0
Control
ZAP
TRIM25
KHNYN
Control
ZAP
TRIM25
KHNYN
HeLa CRISPR
E
ZAP iCLIP - ZMAT3
Normalised crosslink signal
0.03
0.02
0.01
0.00
ATG
STOP
ZMAT3-201 Exons
ZMAT3-203 Exons
20000
40000
ZMAT3 coordinate
F
Mock
HIV-WT
HSPB8 expression
6000
4000
2000
0
Control
ZAP
TRIM25
KHNYN
Control
ZAP
TRIM25
KHNYN
HeLa CRISPR
G
ZAP iCLIP - HSPB8
Normalised crosslink signal
0.04
0.03
0.02
0.01
0.00
ATG
STOP
HSBP8-201 Exons
HSBP8-204 Exons
5000
10000
15000
HSPB8 coordinate

Fig 4

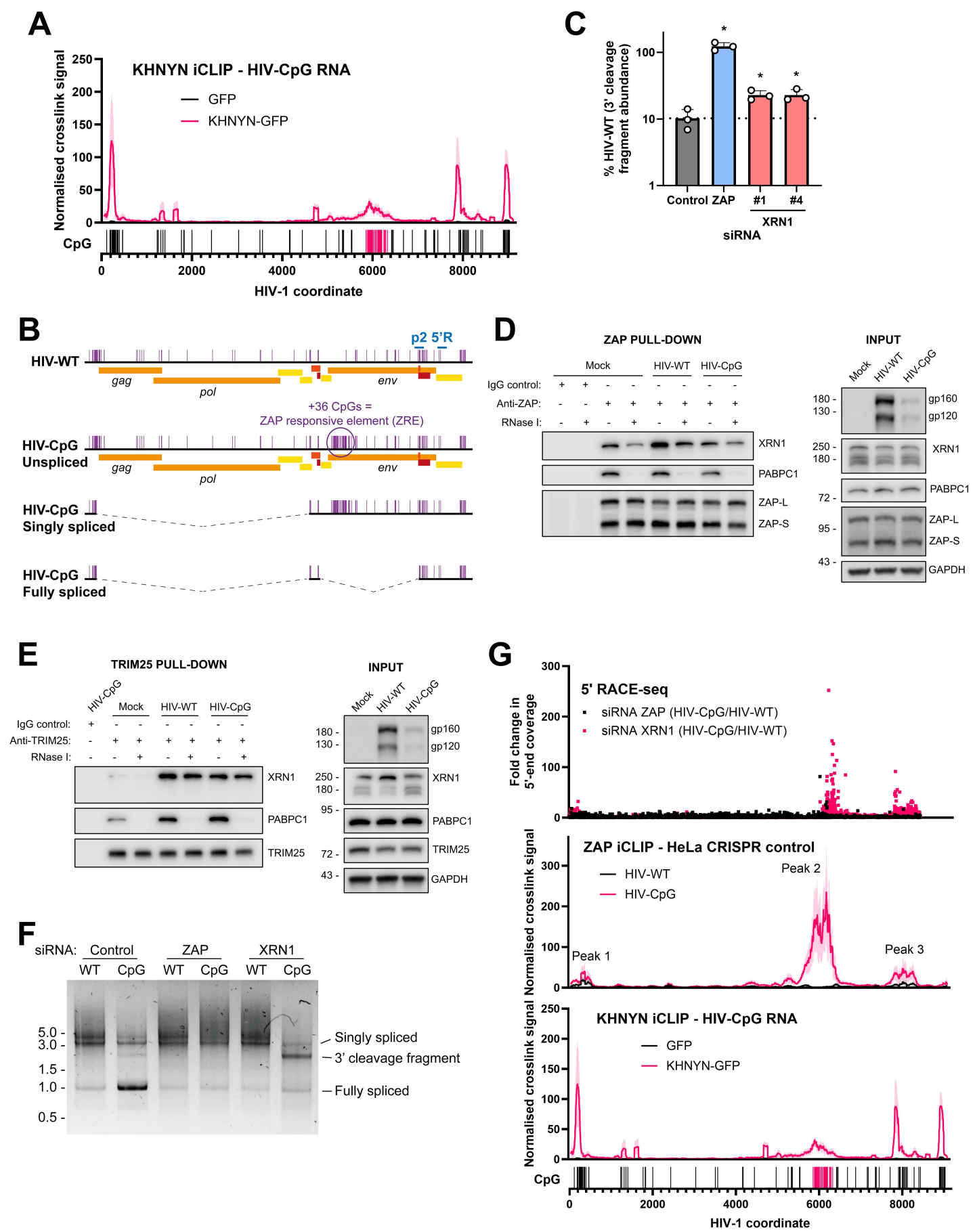
A
KHNYN iCLIP - HIV-CpG RNA
GFP
KHNYN-GFP
Normalised crosslink signal
CpG
HIV-1 coordinate
B
HIV-WT
p2 5'R
gag
pol
env
+36 CpGs =
ZAP responsive element (ZRE)
HIV-CpG
Unspliced
HIV-CpG
Singly spliced
HIV-CpG
Fully spliced
C
% HIV-WT (3' cleavage fragment abundance)
Control
ZAP
#1
#4
XRN1
siRNA
D
ZAP PULL-DOWN
Mock
HIV-WT
HIV-CpG
IgG control:
Anti-ZAP:
RNase I:
XRN1
PABPC1
ZAP-L
ZAP-S
INPUT
gp160
gp120
GAPDH
E
TRIM25 PULL-DOWN
Anti-TRIM25:
TRIM25
F
siRNA:
WT
CpG
Singly spliced
3' cleavage fragment
Fully spliced
G
5' RACE-seq
siRNA ZAP (HIV-CpG/HIV-WT)
siRNA XRN1 (HIV-CpG/HIV-WT)
Fold change in 5'-end coverage
ZAP iCLIP - HeLa CRISPR control
HIV-WT
HIV-CpG
Peak 1
Peak 2
Peak 3
Normalised crosslink signal

Fig 5

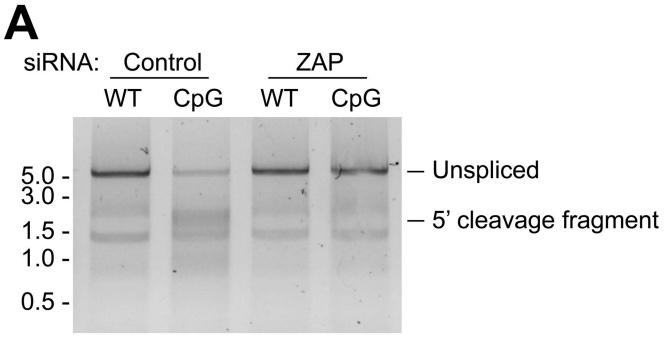

B

3' end position	3' non-templated nucleotides
5686	C
5746	none
5948	none
6196	UUUUU
6284	UUUU
6299	UUUU
6322	U

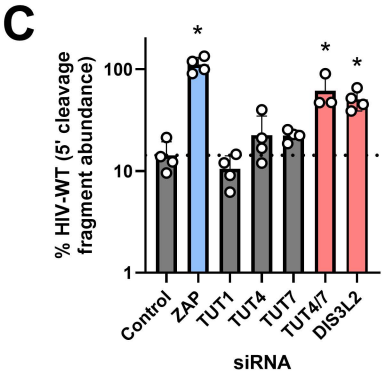

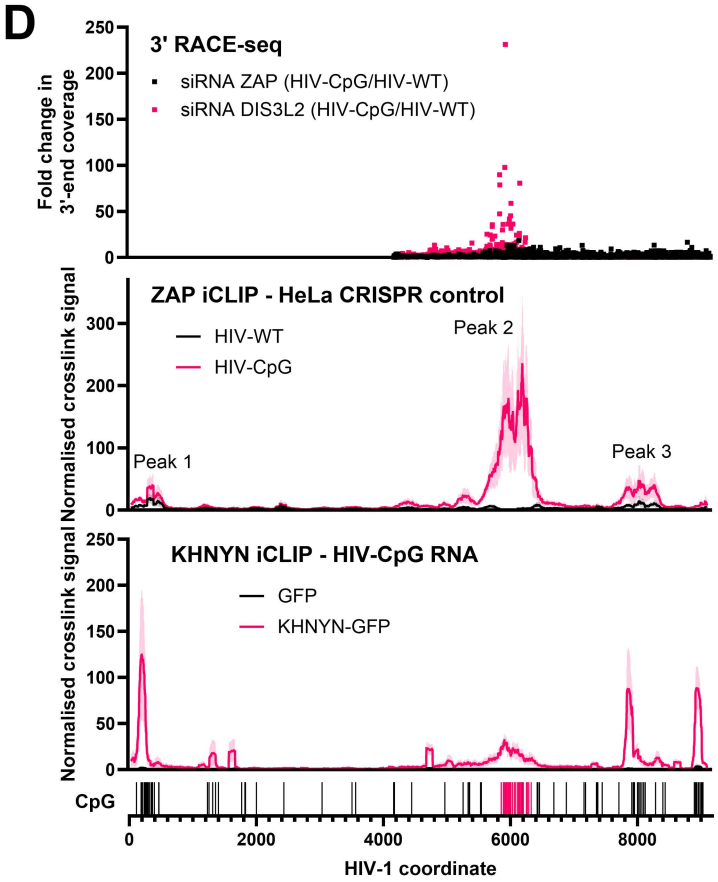

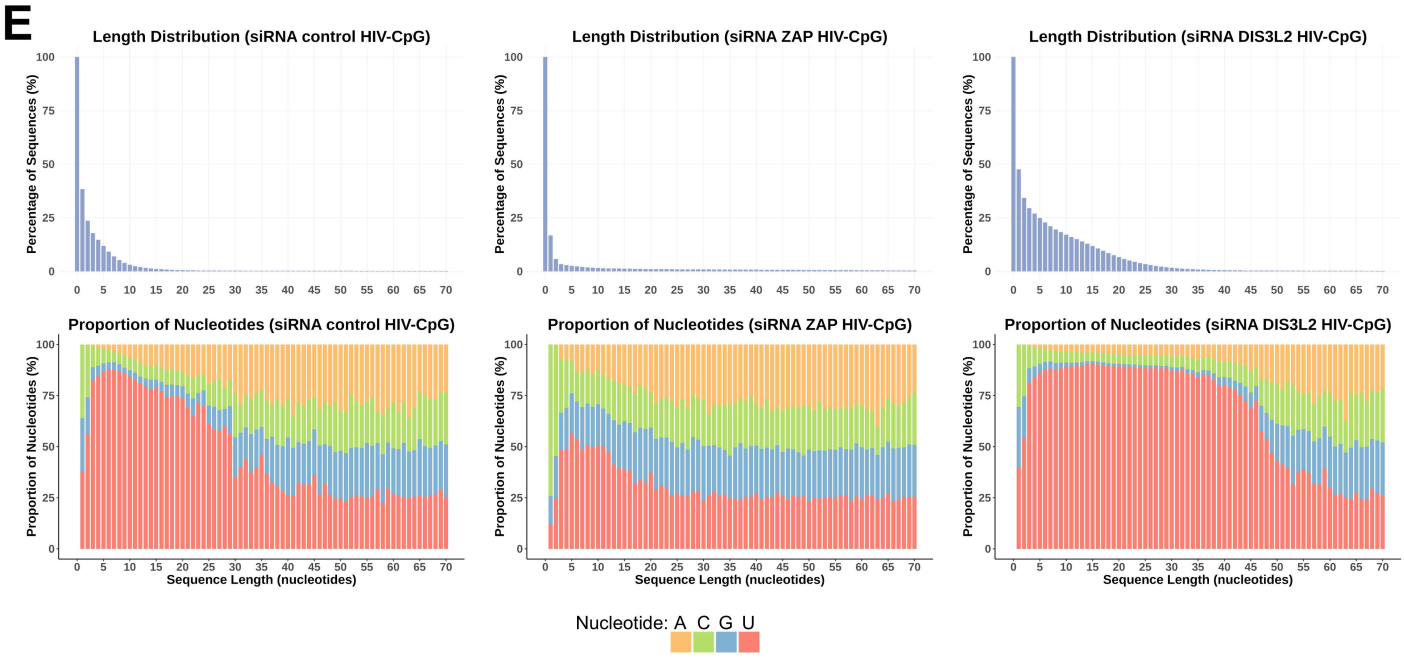

Fig 6

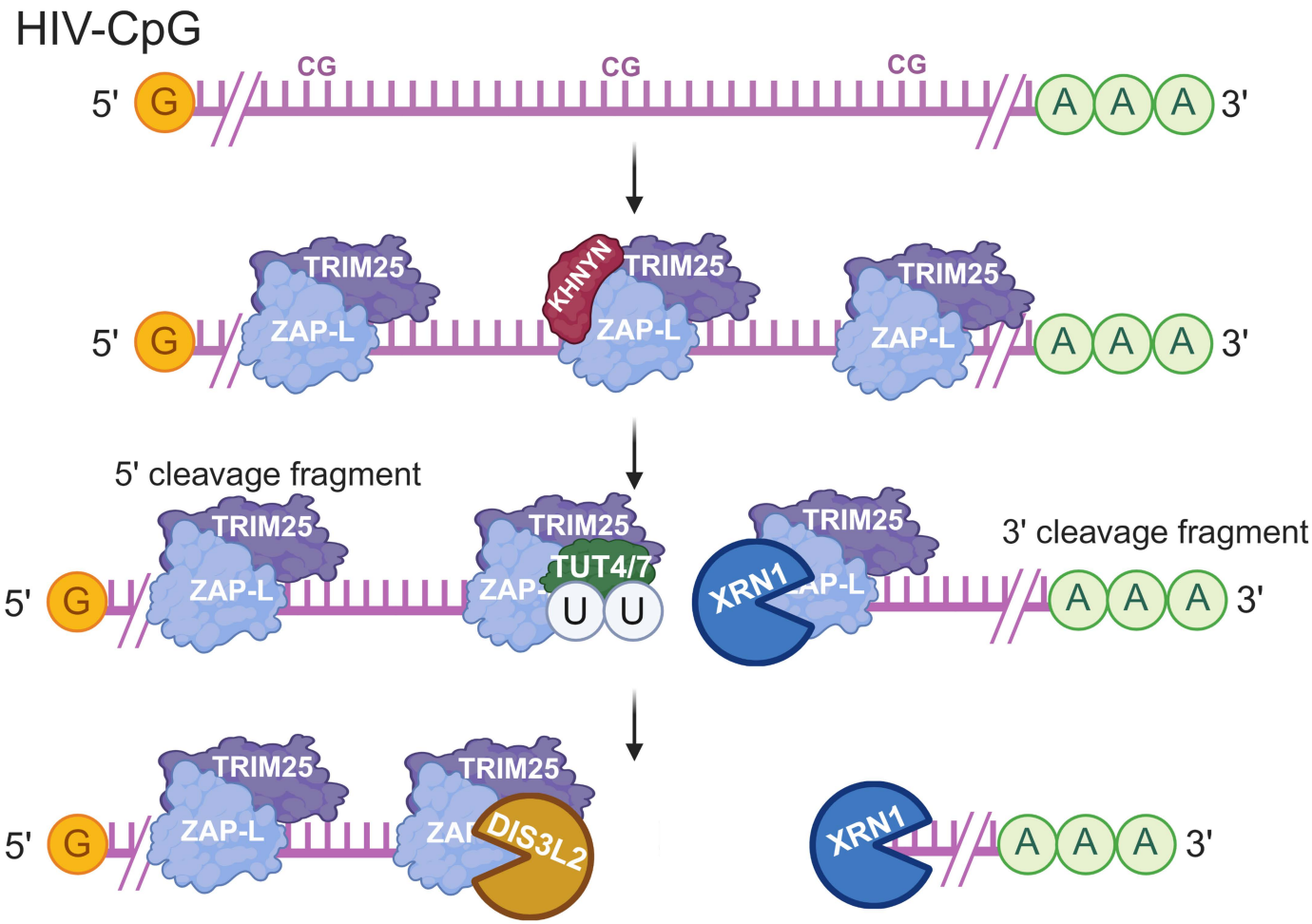
HIV-CpG
5'
G
CG
CG
CG
A A A
3'
TRIM25
ZAP-L
KHNYN
5' cleavage fragment
TUT4/7
U U
XRN1
3' cleavage fragment
DIS3L2

Fig 7